

MATERIALS RESEARCH AT MSFC

July 28, 1966

By

**Charles E. Cataldo
James E. Curry
Raymond L. Gause
James E. Kingsbury
Eugene C. McKannan**

CONTENTS...

	Page
INTRODUCTION TO MATERIALS RESEARCH AT MSFC	
by James E. Kingsbury	1

DIFFUSION BONDING OF DISSIMILAR METALS

	Page
by Charles E. Cataldo	
SUMMARY	3
INTRODUCTION	3
DIFFUSION BONDING	3
Joining Methods	3
Diffusion Aids	3
Diffusion Process	4
Tank Construction and Testing	4
CONCLUSION	6

LIST OF TABLES

Table	Title	Page
I.	Summary of Mechanical Test Results	4
II.	Summary of 50.8-cm (20-in.) Diameter Tank Tests	5
III.	Dissimilar Alloy Combinations	6
IV.	Advantages and Disadvantages of Diffusion Bonded Dissimilar Joints	6

LIST OF ILLUSTRATIONS

Figure	Title	Page
1.	Schematic of Mechanical and Diffusion Bonded Joints	3
2.	Differential Thermal Expansion Tooling Arrangement for Tubular Joints	4
3.	50.8-cm (20-in.) Diameter 2219-321 Transition Joint	5
4.	Cross Section of Test Tank	5

	Page
STRESS CORROSION	
by Charles E. Cataldo	
SUMMARY	7
SATURN VEHICLE STRESS-CORROSION FAILURES AT MSFC	7
STRESS CORROSION FAILURE STUDIES	10
TESTING FOR STRESS CORROSION FAILURE SUSCEPTIBILITY	11
CONCLUSION	13

LIST OF TABLES

Table	Title	Page
I.	Stress Corrosion Evaluation of AM-355 Stainless Steel	10
II.	Summary Comparison of the Effectiveness of Coatings	11
III.	Approximate Threshold Stress of Aluminum Alloys	12
IV.	Stress Corrosion Susceptible and Resistant Alloys	13

LIST OF ILLUSTRATIONS

Figure	Title	Page
1.	LOX Dome on H-1 Engine	7
2.	Two Views of H-1 Engine LOX Dome	8
3.	Crack in LOX Inlet of Dome (Service Failure)	8
4.	Crack in LOX Inlet of LOX Dome (Salt Spray Exposure)	8
5.	Microstructure of Crack in Dome from Engine (Mag. 200X)	8
6.	Cross Section of Flared Tube Fitting	9
7.	Cracks in Sleeves Removed from Service	9
8.	Microstructures of Heat Treated AM 355 (Mag. 500X)	10
9.	Use of Wave Spring in MF Fitting	10
10.	Alternate Immersion Tester	12
11.	Grain Orientation in Aluminum Sheet	12

	Page
EVALUATION OF MATERIALS BY NON-DESTRUCTIVE MEANS	
by Raymond L. Gause	
SUMMARY	15
LIST OF SYMBOLS	15
INTRODUCTION	16
EXPERIMENTAL METHODS FOR DETECTING STRESS CORROSION	16
STRESS ANALYSIS	17
CONCLUSION	21

LIST OF TABLES

Table	Title	Page
I.	Acoustic Velocity Data	17

LIST OF ILLUSTRATIONS

Figure	Title	Page
1.	Approach to Stress-Corrosion Problem	16
2.	(a) Distortional Wave Propagation in an Anisotropic Medium and (b) the Resulting Particle Motion	18
3.	Stress-Induced Birefringence in Cold-Worked 6061-T6 Aluminum	18
4.	Crystallite Preferred Orientation in a Sheet of Rolled Metal	18
5.	Wave Birefringence Caused by Preferred Orientation in Rolled Metal Sheet	18
6.	Aluminum (111) Pole Figure	19
7.	Basic Orientation Produced in Cold-Rolled 6061-T6 Aluminum	19
8.	The Components of Stress for a Rectangular Cartesian Coordinate System	19

MATERIAL DESIGNS FOR ELECTRONIC APPLICATIONS

by Eugene C. McKannan and James E. Curry		Page
SUMMARY		23
DC MOTOR BRUSHES		23

CONTENTS (Continued)...

	Page
DIELECTRICS FOR WIRE COATING	27
ELECTRICAL PROPERTIES OF CRYOGENIC FLUIDS	28
POTTING COMPOUNDS	30

LIST OF TABLES

Table	Title	Page
I.	Motor Brushes at 2000 rpm in Vacuum Environment of 1.33×10^{-6} N/m ² , 300° K (10^{-8} mm Hg, 80° F)	24
II.	DC Motor Generator Evaluations in Environment of 1.33×10^{-4} N/m ² (10^{-6} mm Hg)	27
III.	Mechanical Wire Coating Properties	28
IV.	Electrical Wire Coating Properties	28
V.	Required Properties for Potting Compounds and Conformal Coatings	31

LIST OF ILLUSTRATIONS

Figure	Title	Page
1.	Resistivity vs. Temperature of Brush Materials	24
2.	Run-In Parameters	25
3.	Wear Rate vs. Velocity	26
4.	Wear Rate vs. Current	26
5.	Brush Noise	26
6.	60 Hz Breakdown in Cryogens	29
7.	Gaseous Breakdown	29
8.	Liquid Breakdown	29
9.	Cordwood Module in Potting Compound	30
10.	Printed Circuit Board with Conformal Coating	30
11.	Novel Curing Agents for Conventional Epoxies	32
12.	Epoxy-Silicone Polymers	32
13.	Urethane-Silazane Polymers	33

	Page
NON-METALLIC MATERIALS	
by James E. Curry	
SUMMARY	35
CRYOGENIC INSULATION DEVELOPMENT	35
ADHESIVES RESEARCH	40
MEMBRANE DIFFUSION THEORY	43
REFERENCES	48

LIST OF TABLES

Table	Title	Page
I.	Initial Insulation Goals	35
II.	Performance of Multilayer Insulations	40
III.	Adhesives Research	41

LIST OF ILLUSTRATIONS

Figure	Title	Page
1.	Reflective Multilayer Insulation Materials	36
2.	Insulation Application Process	37
3.	Foam Spacers Separating Insulation Layers	37
4.	Effect of External Compression on Apparent K for Multilayer Insulations	38
5.	Effect of External Compression on $K\rho$ for Multilayer Insulations	38
6.	Effect of External Compression on $Q\rho$ for Multilayer Insulations	39
7.	Cylindrical Calorimeter	40
8.	Tape Wrapped Multilayer Insulations	40
9.	Lap Shear Specimens (NARMCO 7343/7139) Aged at 311° K (100° F); 100% Humidity	41
10.	Lap Shear Specimens (NARMCO 7343/7139) Aged at 311° K (100° F); 100% Humidity	42
11.	Lap Shear Specimens (NARMCO 7343/7139) Aged at 311° K (100° F); 100% Humidity	42
12.	Lap Shear Specimens (NARMCO 7343/7139) Aged at 294° K (70° F); 100% Humidity	42

CONTENTS (Concluded) . . .

Figure	Title	Page
13.	Lap Shear Specimens (NARMCO 7343/7139) Aged in Ambient Outdoor Environment	43
14.	Distribution of Room Temperature Strengths (NARMCO 7343/7139)	43
15.	Distribution of 339° K (150° F) Lap Shear Strengths (NARMCO 7343/7139)	43
16.	Diffusion Through Membranes	44
17.	Fourier Mass Transfer Solution	45
18.	Time Lag Approach	46
19.	Graphical Significance of Time Lag	46
20.	Fick's Second Law for Concentration-Dependent Diffusion Coefficient (D)	46
21.	Holstein Transformation Valid for Short Time Measurements	47
22.	Frisch Time Lag Equations for D Varying with C	47

INTRODUCTION TO MATERIALS RESEARCH AT MSFC

By

James E. Kingsbury

The overall mission of the Materials Division is to support the Saturn Program. In addition, progress continues on actively pursuing the development of inflight experiments necessary to support the Apollo-Saturn Program and the Apollo Applications Program. Included in this effort is the responsibility to anticipate future needs of the space exploration effort. This work permits the investigation of a variety of potential materials developments, and some results of this effort will be discussed. The complexities involved in a successful materials development program are not always apparent. Materials that take months or years to develop are quickly accepted. The technology and experimentation required to develop a reliable adhesive will first require considerable design time and learning the proper adhesive

application process. Likewise, materials with induced stresses and in corrosive environments present a challenge to the Materials Division to develop new materials and applications to prevent stress-corrosion failures. Thus, the elimination of stress-corrosion failures depends partially on decreasing the stress produced by forming, joining, and material assembly operations to include isolating the materials from a corrosive environment. For the present, efforts must be concentrated on eliminating these failures by first understanding the fundamental mechanisms that contribute to the stress-corrosion failures. The Materials Division also has the advantage of being able to capitalize on the available industrial research potential to achieve these goals.

DIFFUSION BONDING OF DISSIMILAR METALS

By

Charles E. Cataldo

SUMMARY

A study of metal joining methods led to the diffusion bonding process using diffusion bonding aids. The diffusion bonding process and construction of diffusion bonded dissimilar metal joints are briefly described. Construction of four tank assemblies by the diffusion bonding process was followed by cycling and burst tests to determine the strength of the bonded joints. Test results on the four tanks are discussed and related to the general use of diffusion bonded alloy combinations.

INTRODUCTION

To provide a potential means of reducing the weight and realizing certain other advantages in propellant ducting components in the Saturn V vehicle, a reliable method for joining aluminum alloy 2219 to type 321 stainless steel in cylindrical form was needed. To meet this objective, an experimental program was conducted by The Boeing Company, Seattle, Washington, under the technical direction of the Materials Division of the Propulsion and Vehicle Engineering Laboratory. The program was to provide a joint that could be bonded as a unit and then welded into the duct system without the use of mechanical joints, as shown in Figure 1.

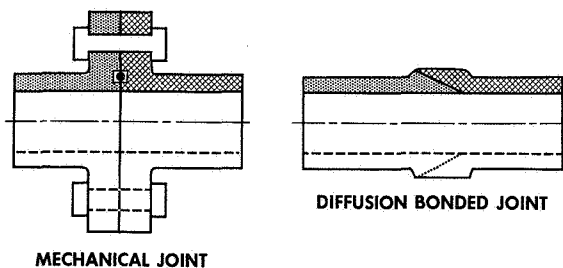


FIGURE 1. SCHEMATIC OF MECHANICAL AND DIFFUSION BONDED JOINTS

DIFFUSION BONDING

JOINING METHODS

A number of potential joining methods and the problems associated with each of these methods were studied. The most promising methods, including brazing, fusion welding, and diffusion bonding were selected for limited evaluation by metallographic examination, mechanical property tests, and corrosion tests. The two most promising methods, fusion welding and diffusion bonding, were then further evaluated by assembling and testing sub-scale 20.8-cm (8-in.) diameter burst test cylinders. The most promising method selected from this phase was diffusion bonding. This method was then used to fabricate 50.8-cm (20-in.) diameter tank assemblies under production conditions. Thermal shock, pressure cycling, leak tests, and burst tests were conducted at room temperature and at 77.5°K (-320° F) on the 50.8-cm (20-in.) diameter tank assemblies.

Although use of the brazing or fusion welding process was considered technically feasible for making tubular joints, these processes were found to have limitations because embrittling layers were formed at the joint interfaces. Widely different physical properties, such as the coefficient of thermal expansion and melting, would be expected to present metallurgical and processing difficulties, particularly when large diameter tank assemblies are required. The diffusion bonding process offered the most potential for making the desired joints.

DIFFUSION AIDS

Since high deformation would be required when bonding materials in their natural state, the use of diffusion aids was evaluated in an attempt to obtain good bonds without excessive deformation of the aluminum alloy member. Copper and silver plating diffusion aids were evaluated. Silver plating, in conjunction with conventional pretreatments designed to insure proper plating adherence, provided

optimum joint characteristics. Tests demonstrated that this plating has excellent resistance to oxidation and a high resistance to contamination.

DIFFUSION PROCESS

Preproduction development work was conducted on flat specimens to establish basic processing parameters. The significant processing parameters that provided the best strength and ductility were as follows: (1) The 321 stainless steel and 2219 aluminum alloy components were electroplated with 0.00127-cm (0.0005-in.) thick silver. (2) Just prior to bonding, the electroplated surfaces were abraded lightly with 240-grit sandpaper and then cleaned with acetone. (3) Using an air atmosphere furnace, specimens were held at 533°K - 589°K (500° F - 600° F) for two to four hours under pressure sufficient to cause compressive yielding that was obtained using a pressure of $1.38-1.72 \times 10^8$ N/m² (20-25 ksi). Deformation occurs in the aluminum thickness and no significant deformation occurs in the stainless steel. Single and double lap shear specimens were tested at room temperature, at 77.5°K and at 20.4°K (-320° F and -423° F). Test results are shown in Table I. Typically, shear strength at room temperature exceeds 1.033×10^8 N/m² (15 000 psi), with 20 to 30% increases, respectively, at 77.5°K and at 20.4°K (-320° F and -423° F).

TABLE I. SUMMARY OF MECHANICAL TEST RESULTS

Type Specimen	Stress, N/m ² × 10 ⁸ (psi)		
	298°K (77° F)	77.5°K (-320° F)	20.4°K (-423° F)
Double Lap	1.000 (14 500)	1.085 (15 750)	1.410 (20 450)
	1.092 (15 880)	1.279 (18 550)	1.420 (20 600)
	0.984 (14 280)	1.441 (20 900)	1.655 (24 000)
Single Lap	1.219 (17 690)	1.310 (19 000)	1.371 (19 900)
	1.131 (16 410)	1.263 (18 310)	1.442 (20 930)
	1.090 (15 800)	1.603 (23 250)	1.120 (16 250)

TANK CONSTRUCTION AND TESTING

The processing parameters established during the preproduction development were applied in making 50.8-cm (20-in.) diameter tank assemblies. Pressure was controlled by using a differential thermal expansion apparatus. Figure 2 is a simplified

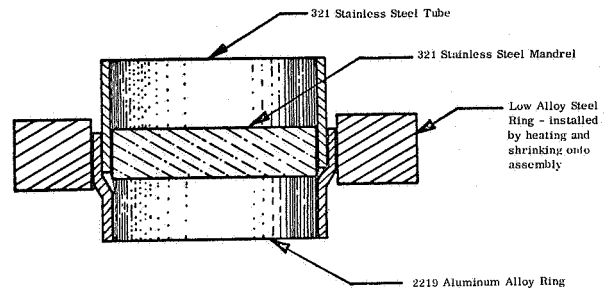


FIGURE 2. DIFFERENTIAL THERMAL EXPANSION TOOLING ARRANGEMENT FOR TUBULAR JOINTS

schematic tooling arrangement. The inner mandrel of the 321 stainless steel has a linear thermal expansion between room temperature and 755° K (900° F), approximately 50% greater than that of the T-1 steel outer mandrel. Calculations revealed that the 50.8-cm (20-in.) inner stainless steel ring has a free diametric expansion approximately 0.762 cm (0.30 in.) greater than the low alloy steel restraining ring at 589°K (600° F). However, during actual bonding, the compressive pressure from the restraining ring would prevent this total expansion from occurring; likewise, the bonding pressure places the external alloy steel ring in hoop tension and results in expanding to a greater diameter than would occur on its free expansion at 589°K (600° F). Calculations showed that to create an internal bonding pressure which approximates the compressive yield strength of the 2219-T62 alloy, the outer restraining ring must be installed using a shrink-fit. This interference fit is required to provide the preload to supplement the pressure from the differential expansion of the tooling.

Figure 3 shows a typical 50.8-cm (20-in.) diameter transition joint. Four transition joints were prepared and tested by helium leak checking and thermal shocking between room temperature and 77.5°K (-320° F). Each unit successfully passed the thermal shock test which consisted of ten cycles between room temperature and 77.5°K (-320° F). Each transition joint was welded into a tank as shown in Figure 4, and a helium leak check was made.

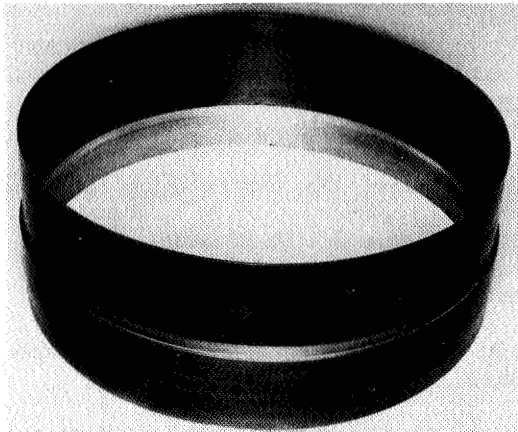


FIGURE 3. 50.8-cm (20-in.) DIAMETER 2219-321 TRANSITION JOINT

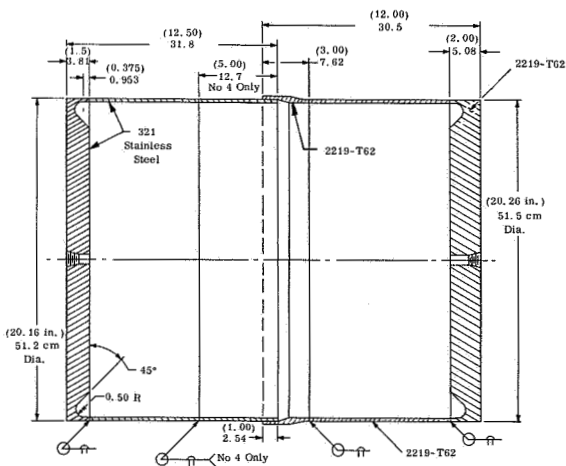


FIGURE 4. CROSS SECTION OF TEST TANK

The tanks were leak tight except for tank assembly number 2, which exhibited a leak in the joint. This leak was attributed to insufficient pressure during the bonding cycle because of shrinkage of the inner mandrel during processing. This situation was corrected on the third and fourth assemblies.

The tanks were pressure cycled at room temperature and 77.5° K (-320° F) followed by burst testing. The chart in Table II summarizes the test results. The first tank successfully passed

TABLE II. SUMMARY OF 50.8-cm (20-in.) DIAMETER TANK TESTS

Tank No.	Test Method	Cycle Pressure N/m ² × 10 ⁶ (psig)	Number Cycles	Burst Pressure N/m ² × 10 ⁶ (psig)	Pr _t N/m ² × 10 ⁸ (psi)
1	Water at Room Temperature	2.41 (350)	200	3.24 (470)	2.590 (37 600)
2	LN ₂ (-320° F) 77.5° K	2.41 (350)	85 (Failed)	-	1.930 (28 000)
3	LN ₂ (-320° F) 77.5° K	2.41 (350)	92	3.48 (505)	2.785 (40,400)
4	LN ₂ (-320° F) 77.5° K	2.135 (310) 1.655 (240)	60 140	4.62 (670)	3.695 (53 600)

1 Based on 0.318-cm (0.125-in.) Aluminum Wall Thickness

2 Cycling Pump Failed on 92nd Cycle

pressure cycling of two-hundred cycles at 2.41×10^6 N/m² (350 psig). The tank failed at 3.24×10^6 N/m² (470 psig) in the room temperature burst test. The second assembly was pressurized with liquid nitrogen and failed during the 82nd pressure cycle at 2.41×10^6 N/m² (350 psig).

This tank had only compressively yielded 0.0025-0.0050 cm (0.001-0.002 in.) because of insufficient pressure during bonding. This was attributed to shrinkage of the inner mandrel during the processing of assemblies numbers 1 and 2 as discussed previously. Earlier work had indicated that at least 0.010 cm (0.004 in.) compressive yielding of the aluminum was required for sound joints.

The third tank passed the pressure cycling test using liquid nitrogen as the pressurizing medium. The tank had been subjected to 92 cycles at 2.41×10^6 N/m² (350 psig) when the cycling pumps failed. The cycling test was terminated at that point, and the burst test was conducted. The tank failed at 3.48×10^6 N/m² (505 psig) at 77.5° K (-320° F).

The fourth and final tank assembly was fabricated using the experience gained from the first three assemblies, and hence provided the best results. This assembly successfully passed a two-step cycling test of 60 cycles at 2.135×10^6 N/m² (310 psig) and 140 cycles at 1.655×10^6 N/m² (240 psig) using liquid nitrogen as the pressurizing medium. The tank ruptured at 4.62×10^6 N/m² (670 psig) during the burst test. This pressure corresponds to a hoop stress of 3.695×10^6 N/m² (53 600 psig).

Peel loading caused by deformation of the aluminum alloy contributed to failure initiation in all cases. Redesign of the joints to provide a slight increase in wall thickness of the aluminum alloy member should significantly decrease the peel loading and result in higher burst pressures. By proper joint design, the joint can be made to be as strong as the base metal.

Additional diffusion bonding studies are being conducted on other alloy combinations. The influence of the primary diffusion parameters of time, temperature and pressure will be studied along with examining the process variables such as surface preparation, atmosphere and intermediate materials. Both solid state joining and press and roll bonding are being studied for the six combinations in Table III.

CONCLUSION

Based on studies that have been completed to date, all alloy combinations listed in Table III can be bonded without surface coatings or intermediates; however, better joint strength and metallurgical characteristics can be obtained by using diffusion aids. Designers should take advantage of this previously unfeasible process of joining dissimilar metals (Table IV). Experience gained to date has indicated that there

are only few limits on the alloy combinations that can be joined by diffusion bonding.

TABLE III. DISSIMILAR ALLOY COMBINATIONS

(1)	2219 Aluminum Alloy to 5 Al - 2.5 Sn Titanium Alloy
(2)	2219 Aluminum Alloy to 321 Stainless Steel
(3)	7106 Aluminum Alloy to 321 Stainless Steel
(4)	Inconel 718 Alloy to 321 Stainless Steel
(5)	8 Al - 1 Mo - 1V Titanium Alloy to 321 Stainless Steel
(6)	Inconel 600 Alloy to 8 Al - 1 Mo - 1Y Titanium Alloy

TABLE IV. ADVANTAGES AND DISADVANTAGES OF DIFFUSION BONDED DISSIMILAR JOINTS

<u>Advantages</u>	
	Weight Saving
	No Seal Problem
	No Distortion during Fabrication
	Heat Treated or Cold Worked Temper can be Retained
	Control over Formation of Brittle Intermediate Phases
	Compact Design
<u>Disadvantages</u>	
	Close Control over Processing Parameters Required
	Corrosion Possible if Joint not Protected

STRESS CORROSION

By

Charles E. Cataldo

SUMMARY

This article recounts briefly some of the more critical stress-corrosion failures that have been experienced at Marshall Space Flight Center and the corrective action taken. Some of the recent stress-corrosion studies are described and preliminary results tabulated. Specific problems described are the H-1 Engine LOX dome, the pneumatic line fitting sleeve problems and the more recent problem with wave springs used on MF-flared tube fittings. The use of nitric oxide in preventing stress-corrosion failures in titanium tanks is also discussed.

SATURN VEHICLE STRESS-CORROSION FAILURES AT MSFC

Stress-corrosion failures of high-strength metal aerospace components have occurred on the H-1 engine. The LOX dome is the forward closure on the H-1 engine combustion chamber through which liquid oxygen enters the injector (Fig. 1, 2). The dome was fabricated initially from a 7079-T6 aluminum die forging. In 1960 a dome was found cracked on the Saturn I, and later other domes cracked. Figure 3 shows a typical crack in one of these domes, and for a comparison, Figure 4 shows a dome exposed to salt spray for 24 days. The intergranular stress-corrosion cracking that is typical of most high strength aluminum alloys is shown in Figure 5.

Other than having a susceptible material to begin with, three conditions are necessary for stress-corrosion failures to occur. These are tensile stresses on the surface, a corrosive medium and time for the failure to develop. A check of the manufacturing sequence of this LOX dome indicated that the material was forged, heat treated and machined. After being heat treated, this type of forging is in a highly stressed condition because of its forged shape and the quench operation. Generally, such a forged part contains high residual compressive stresses on the surface and high tensile stresses

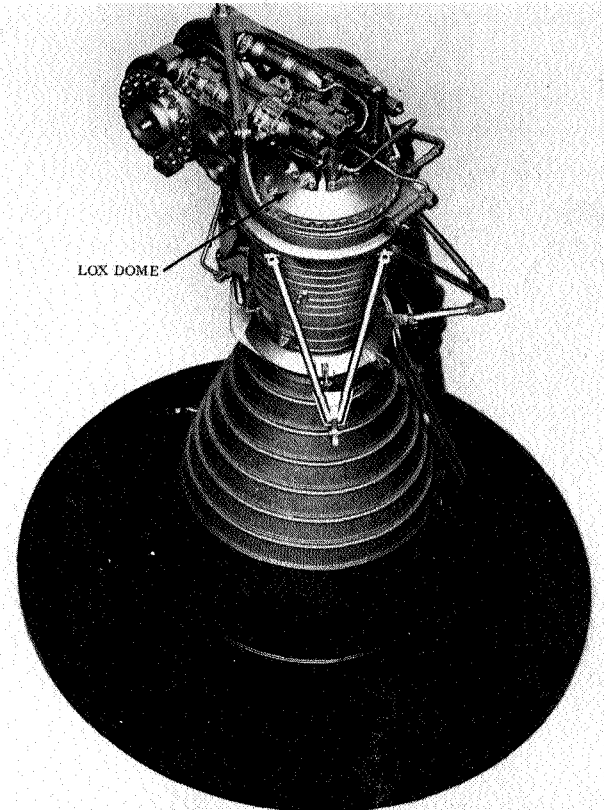


FIGURE 1. LOX DOME ON H-1 ENGINE

within. This results from rapid cooling of the surface in the quench process and differential cooling of the center of the cross section. The center of the forging cools last, and contraction tends to pull the surface and produce compressive stresses. Subsequent machining removes the compressively stressed material and exposes material under high tensile stresses. These factors, coupled with sufficient time and exposure to atmospheric conditions that constitute the corrosive medium, are likely to result in stress-corrosion failure.

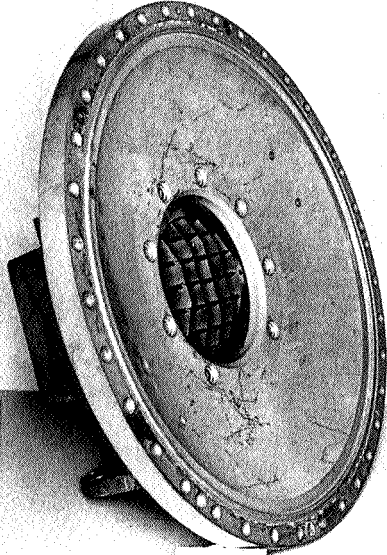
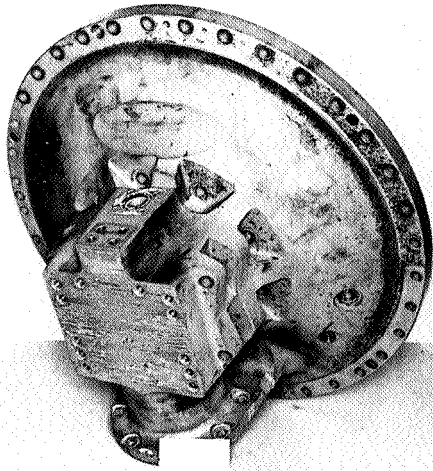


FIGURE 2. TWO VIEWS OF H-1 ENGINE LOX DOME

The LOX domes were reworked following the initial failures. The modification consisted of (1) stripping the anodized coating, (2) reheat-treating to T6 condition, (3) finish machining to correct any out-of-tolerance condition resulting from heat treatment, (4) shot peening surfaces and pressure rolling inside of bolt holes, (5) honing the sealing surfaces, and (6) re-anodizing and painting.

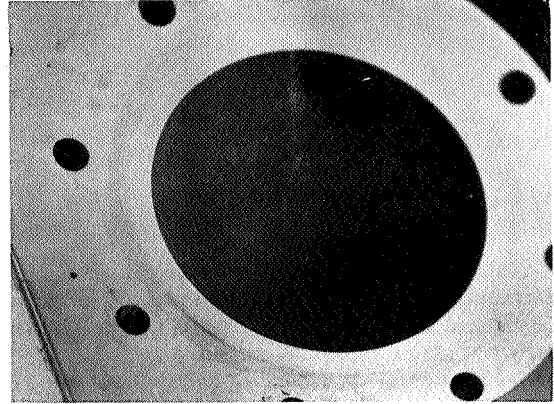


FIGURE 3. CRACK IN LOX INLET OF DOME (SERVICE FAILURE)

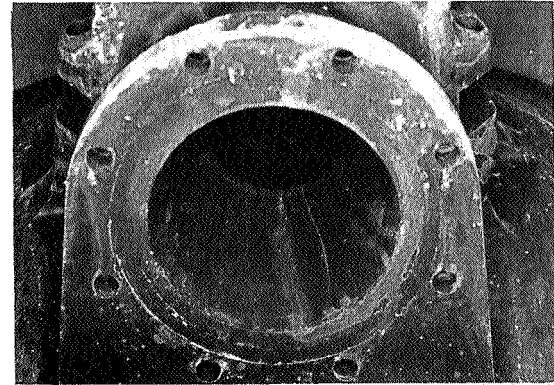


FIGURE 4. CRACK IN LOX INLET OF LOX DOME (SALT SPRAY EXPOSURE)

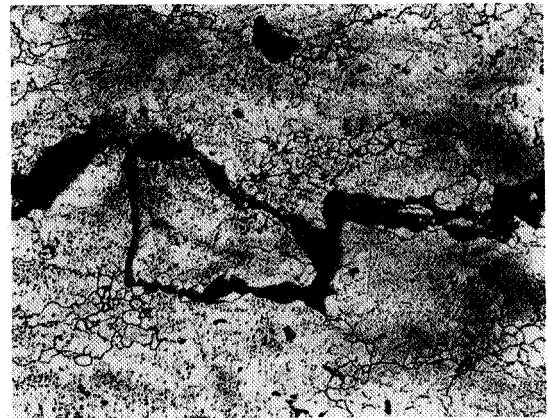


FIGURE 5. MICROSTRUCTURE OF CRACK IN DOME FROM ENGINE (MAG. 200X)

Since the 7079-T6 alloy was known to be highly susceptible to stress-corrosion cracking, steps were taken to initiate fabrication of the domes from 7075-T73 aluminum alloy that is practically immune to stress-corrosion cracking. Reworking the 7079-T6 LOX domes prevented failure until one of these modified domes failed on the Saturn I vehicle SA-7 (1964). By this time the domes being fabricated from 7075-T73 were ready for use. These new domes were immediately installed and have been satisfactory to date.

The stress-corrosion failures of the sleeves used on flared pneumatic tube fittings and on the wave springs used on MF type fittings were similar, because in both cases the failures were caused by stresses applied by torquing the fittings rather than by the residual stresses caused by the heat-treating operation.

The tubing sleeves (Fig. 6) were fabricated from AM-355 stainless steel. Sleeves of this design

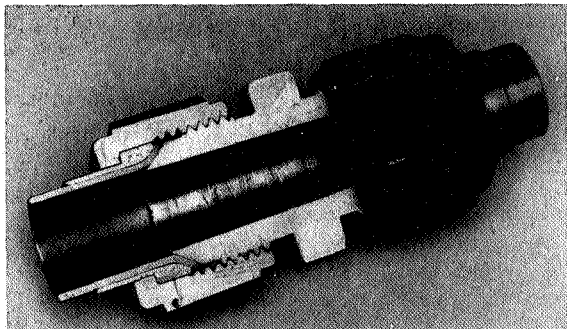


FIGURE 6. CROSS SECTION OF FLARED TUBE FITTING

have been made from a variety of materials for several years and problems with cracking have been attributed to various reasons such as poor machining techniques, improper fit, inclusions in the material and poor flaring techniques. In this case, however, the problem was attributed to stress-corrosion cracking.

The typical failure mode of the tubing sleeves is shown in Figure 7. AM 355 stainless steel is a precipitation hardening alloy, and under certain conditions is quite susceptible to stress-corrosion cracking. The heat treatment used is the most

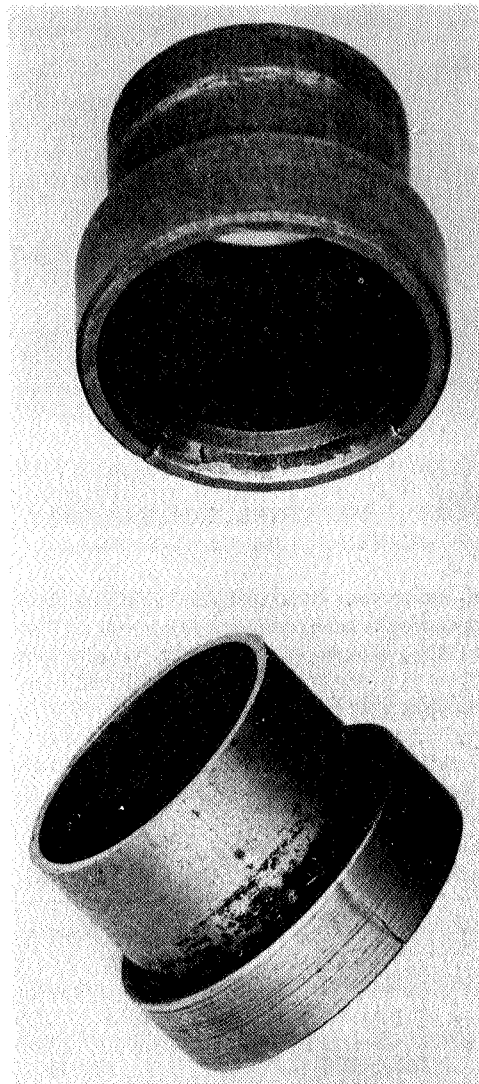


FIGURE 7. CRACKS IN SLEEVES REMOVED FROM SERVICE

important factor in controlling this phenomenon. An intensive stress-corrosion study of the sleeve material revealed that the alloy was susceptible to stress-corrosion cracking in the particular heat treatment that was being used (SCT 1000), and was almost immune to stress-corrosion cracking in the fully hardened (FH) SCT 1000 heat treatment that involved an additional step in the heat treatment and minimized the formation of carbide particles in the grain boundaries of the material.

A comparison of the microstructure of SCT-1000 and FH SCT-1000 is shown in Figure 8. The results

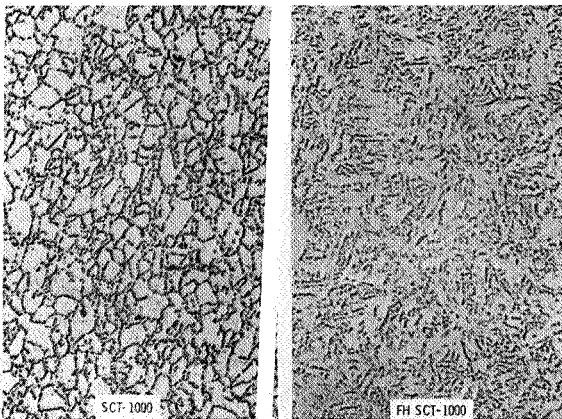


FIGURE 8. MICROSTRUCTURES OF HEAT TREATED AM 355 (MAG. 500X)

of a study on various heat-treated conditions under different exposure environments are given in Table I. All existing sleeves for the Saturn vehicle were reheat-treated to the fully hardened (FH) SCT-1000 heat treatment with very good results.

TABLE I. STRESS CORROSION EVALUATION OF AM-355 STAINLESS STEEL

Heat Treatment	Stress % Y. S.	Failure / Tests	Days to Failure Range
SCT 850	25-100	12/12	2-114
SCT 1000	25-100	14/24	30-156
FHSCT 850	25	0/6	NF (180)
	50-100	7/18	151-152
FHSCT 900	25-50	0/6	NF (180)
	75-100	3/6	97-156
FHSCT 950	25-100	0/12	NF (180)
FHSCT 1000	25-100	0/24	NF (180)

Figure 9 shows the use of a wave spring in an MF type fitting. The spring is used to force a retainer with ratchet teeth against the fitting nut to maintain a preset torque. The wave spring problem was similar to the sleeve problem in that tensile stresses were introduced into the part by torquing the flared tube fitting. A precipitation-hardening alloy (17-7pH) was involved. Although tests

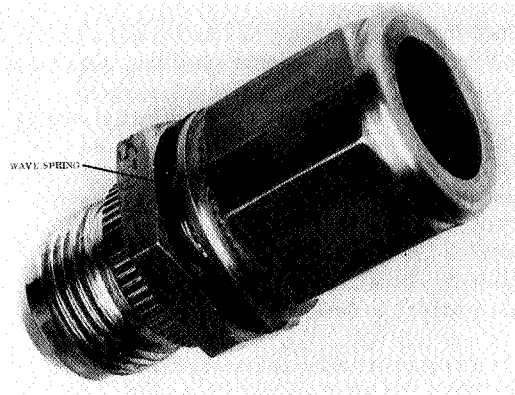


FIGURE 9. USE OF WAVE SPRING IN MF FITTING

indicated that the stress-corrosion susceptibility of this alloy could be greatly improved by a different heat treatment, the treatment used reduced the strength to a point where it could not be used for this application. The problem was solved by changing to Inconel-718 alloy that was not susceptible to stress-corrosion cracking.

STRESS CORROSION FAILURE STUDIES

The Materials Division has applied maximum effort in the study of the stress-corrosion susceptibility of the alloys presently being used in the Saturn V vehicles and other newer alloys being developed. Contractors were requested to report the use of all alloys susceptible to stress-corrosion cracking. Drawings of these parts have been studied and changes have been recommended where necessary.

In the past year many aerospace organizations have increased their work in stress-corrosion studies. Although few conclusive facts have been established regarding the true mechanism of this phenomenon, the fact that more people have become aware of the problem has had a major effect in reducing failures. Thus stress corrosion can be prevented by careful attention to the choice of alloys and tempers and especially by strict adherence to good design and assembly practices.

The four primary conditions that contribute to stress-corrosion failures were used as guidelines to formulate the matrix of the stress-corrosion evaluation program within the Materials Division.

These conditions are (1) susceptible material, (2) tensile stresses, (3) environment, and (4) time. The combination of these conditions will result in stress-corrosion failures, providing the relative weight of just the right combination is sufficient. For most of our space vehicle applications the variables of corrosive environment and time cannot be regulated. Therefore, considerable emphasis has been placed on controlling the materials and the tensile stresses involved.

As was indicated in the examples of the stress-corrosion problems that have occurred in the Saturn S-I and S-IC stages, these particular problems were solved by either changing the alloy or the heat treatment. Many potential stress-corrosion problems have been prevented by the appropriate use of coatings, plating, and other surface treatments. This is the simplest form of protection where susceptible alloys must be used because of other considerations. The commonly used treatments include shot peening, galvanic type coatings, organic paints, anodic type coatings and combinations of these processes.

In a recent study, 15 protective systems were selected for evaluation in preventing or reducing the susceptibility of stress corrosion of aluminum alloys. Specimens of alloys known to be highly susceptible to stress corrosion (2014-T651, 7079-T651, 2024-T351 and 7178-T651) were coated with various protective systems, stressed and exposed to four environments, i.e., alternate immersion in a salt solution, an industrial site and two seacoast environments. The overall results are shown in Table II.

TABLE II. SUMMARY COMPARISON OF THE EFFECTIVENESS OF COATINGS

Coating System:
<u>Recommended Systems</u> (0 to 5 Percent Failures)
Shot Peen + Epoxy
7072 Metallized + Epoxy
7072 Metallized
<u>Restricted Applications</u> (35 to 45 Percent Failures)
Zinc Electroplate
Shot Peened
Primer + Epoxy
Primer + Polyurethane
Primer + Al Pigmented Epoxy + Epoxy
<u>Not Recommended</u> (50 to 97 Percent Failures)
Zinc Rich Paint
Epoxy
Polyurethane
Zinc Chromate Primer
Sulphuric Acid Anodize
Hard Anodize

The best protection appears to be the use of a combination of shot peening or metallizing in addition to a top coat of epoxy-polyamide. Of the galvanic type coatings, 7072 metallizing and zinc electroplate, the 7072 metallized aluminum is the preferred coating, but galvanic coatings have many manufacturing disadvantages. Shot peening is capable of providing good protection, provided that all the tension surfaces that are or may be exposed are adequately peened, and severe surface corrosion is not encountered. If surface corrosion is expected, additional protection against general corrosion must be provided to prevent penetration of the compressive layer produced by peening. Shot peening appears most effective when performed after the sustained tension has been introduced. Good protection is also possible from the use of chromate primers plus organic coatings such as epoxy-polyamide or polyurethane paint, providing the paint envelope remains intact and is not broken by inadvertent mechanical damage. The epoxy is the better of the two coatings. Anodic films such as sulphuric acid anodizing are not effective methods of preventing stress-corrosion cracking.

TESTING FOR STRESS CORROSION FAILURE SUSCEPTIBILITY

With respect to determining the resistance of a material to stress-corrosion cracking, the development of aluminum alloys and tempers with a high order of resistance such as 2219-T851 and -T87, and 7075-T73, has generated a need for a rapid test that can be used to screen alloys. Current specifications for such alloys require a 30-day stress-corrosion test by alternate immersion in a 3.5 percent sodium chloride (NaCl) solution. A typical alternate immersion test apparatus is shown in Figure 10. Rapid test procedures are desired and successful methods have been found for testing the 7075-T73 alloy. This method involves conductivity and potential measurement techniques.

The above techniques have not been adequate for 2219 aluminum alloy. Many electrolytes are being investigated in an effort to obtain a corrodent more aggressive than sodium chloride solutions for 2219 alloy. At the present time, a solution containing 3.5 percent NaCl + 0.7 percent chromic acid and 1.0 percent potassium dichromate appears very promising.

Although no major stress-corrosion failures have occurred in welded joints, the change in metallurgy as a result of heating could change the stress-corrosion susceptibility. Localized stresses

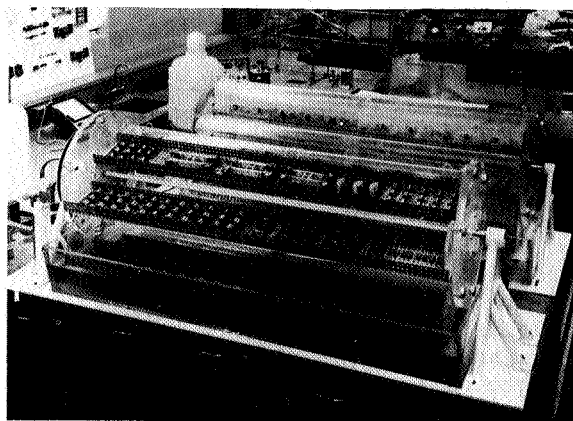


FIGURE 10. ALTERNATE IMMERSION TESTER

are also present in weldments. Considerable work in this area is presently being conducted on aluminum alloys 2219-T87, 2014-T6, and four relatively new high strength weldable alloys, i. e., X7002, X7106, X7039, and X7139. Results of these stress-corrosion tests indicate very good resistance of weldments of all six alloys when stressed to 75 percent of the weld yield strength. While post-weld aging increases the weld strength and decreases the localized corrosion at the heat-affected zone, the resistance to stress corrosion is markedly decreased.

Some additional work has been done in the Materials Division to determine threshold stresses below which stress-corrosion failure of a metal will not occur. There is no specific method, such as calculated rate of corrosion based on weight loss, for classifying materials as to stress-corrosion cracking susceptibility. Some investigators tend to place too much emphasis on relating time to failure in classifying alloys. A representative failure time, i. e., true average, mean failure, median failure, geometric mean failure, is very difficult to obtain and the method of loading has a pronounced effect on failure time. The threshold stress (stress level below which failure is not encountered) appears to be one of the most meaningful methods of comparing materials. Table III gives preliminary test data from a series of tests wherein test specimens were exposed to alternate immersion to 3.5 percent NaCl testing at various short transverse stress levels for nominal periods of 90 days. The indicated threshold stress level gives a relative merit of susceptibility of the material and provides an indication of safe design values. The term "short transverse" has been mentioned in describing several evaluations. Figure 11 illustrates a typical

TABLE III. APPROXIMATE THRESHOLD STRESS OF ALUMINUM ALLOYS

Alloy	Grain Direction	Threshold Stress $N/m^2 \times 10^8$ (ksi)
7001-T75	 Short Transverse	3.45 (50)
7075-T73		3.10 (45)
2219-T8		2.96 (43)
2024-T8		1.72-2.07 (25-30)
2024-T3 & -T4		<1.38 (<20)
2014-T6		<1.03 (<15)
2017-T4		<1.03 (<15)
7039-T61 & -T64		<1.03 (<15)
7106-T6351		<0.69 (<10)
7139-T6351		<0.69 (<10)

2014-T6 ALUMINUM

0.318-cm
(1/8-in.)
SHEET STOCK

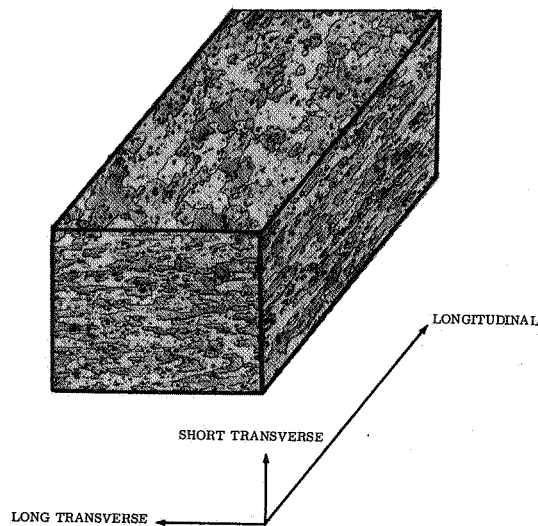


FIGURE 11. GRAIN ORIENTATION IN ALUMINUM SHEET

cross section of 2014-T6 aluminum sheet with the indicated grain directions and corresponding microstructures. Most stress-corrosion evaluations consider primarily the short-transverse grain direction because this is the most susceptible direction for stress-corrosion cracking to occur.

Table IV lists a number of structural alloys with respect to their overall stress-corrosion cracking characteristics. Note that some of the alloys have no temper designations and are considered susceptible or resistant in all tempers, while others are listed

with specific temper designations. This particular listing is representative of some of the major alloys used in the Saturn V system, and the materials listed have been evaluated by exposure to alternate immersion testing in 3.5 percent sodium chloride solution.

TABLE IV. STRESS CORROSION SUSCEPTIBLE AND RESISTANT ALLOYS

SUSCEPTIBLE ALLOYS		RESISTANT ALLOYS	
Aluminum	Steel	Aluminum	Steel
<ul style="list-style-type: none"> ● 2014 ● 2219-T3 & -T4 ● 2024-T3 & -T4 ● 7001-T6 ● 7106 & 7039 ● 7075-T6 ● 7178 ● 7079 ● 195 Casting ● 220 Casting 	<ul style="list-style-type: none"> ● 17-4 PH & 17-7 PH ● AM-350 & AM-355 ● 410 ● Low Alloy Steel at High Strength Levels ● Maraging Steel 	<ul style="list-style-type: none"> ● 3000, 5000, & 6000 Series ● 2219-T6 & -T8 ● 2024-T6 & -T8 ● 7001-T75 ● 7075-T73 ● Most Castings 	<ul style="list-style-type: none"> ● 300 Series ● AM-355, FH SCT 1000 ● A-286 <p style="text-align: center;"><u>Nickel Alloys</u></p> <ul style="list-style-type: none"> ● Inconel 718 ● Waspaloy

So far, major emphasis has been placed on aluminum and stainless steel stress-corrosion problems, but another case involving titanium occurred recently. In July 1965, a 6Al-4V titanium tank used for storage of nitrogen tetroxide (N_2O_4) failed while undergoing a pressure test. An extensive study of N_2O_4 revealed that N_2O_4 of previous manufacture that had been stored for several years would generally not cause cracking of the titanium, whereas N_2O_4 of recent manufacture would cause stressed titanium specimens to fail in a matter of hours. Chemical analysis revealed that the old N_2O_4 contained oxides of nitrogen, predominately nitric oxide (NO). In order to determine whether the nitric oxide was actually inhibiting the cracking, a considerable amount of the old N_2O_4 was purified by passing pure oxygen through the liquid and then vacuum distilling. The purified material was alternately frozen and distilled under reduced pressure several times to remove any highly volatile products. Stressed specimens of titanium exposed to this highly purified material failed in a matter of hours. These studies indicated that nitric oxide

present in amounts of 0.25 percent or more will act as an inhibitor in preventing the cracking. The procurement specification for N_2O_4 was changed to incorporate sufficient NO in N_2O_4 . The addition of NO has no apparent effect on the characteristics of N_2O_4 as a rocket engine propellant. This solution did not involve a change of alloy or temper of the alloy, but rather the use of an inhibitor for stress-corrosion cracking.

CONCLUSION

Although great strides have been made in combating stress corrosion, stress-corrosion failures are still possible. The phenomena of stress-corrosion cracking have been found to be very unpredictable. Carefully machined specimens of a susceptible alloy taken from the same piece of plate, exposed to the same environment and stressed to the same level, may have very random failure times or may not fail. Being able to determine the condition

of a component with regard to stress corrosion during its service lifetime would be of great value. Therefore a number of studies have been initiated to develop nondestructive methods to determine the stress-corrosion susceptibility of a material or component. Several programs have also been awarded

for studying the basic mechanisms and other aspects of stress corrosion. In these studies, such non-destructive techniques as internal friction, electrical conductivity, ultrasonic surface attenuation and acoustic emission techniques are being used.

EVALUATION OF MATERIALS BY NON-DESTRUCTIVE MEANS

By

Raymond L. Gause

SUMMARY

The factors that result in a failure caused by stress corrosion are discussed and the various methods used to detect stress corrosion are mentioned. The role of non-destructive testing in solving the stress corrosion problem is outlined. Experimental techniques that may be capable of detecting and measuring stress corrosion and residual stress are discussed. In addition, equations are given for the ultrasonic wave propagation in an anisotropic medium.

LIST OF SYMBOLS

English Symbols

c_{ij}	the first order elastic constants.
c_{ijkl}	the second order elastic constants.
D_{ij}	the coefficients of the wave equations for an anisotropic body.
$\hat{\epsilon}$	the strain tensor.
e_{kl}	the components of the strain tensor.
F	the fraction of the crystallites in an aggregate which are oriented in the most preferential way.
h	the thickness of the elastic medium parallel to the direction of propagation.
K	the ratio of the angular frequency to the wave velocity.
l_1 l_2 l_3	the direction cosines of the normal to the wave front.
\hat{T}	the strain tensor.

T_{ij}	the components of the strain tensor.
t	time.
t_1	the specimen transit time for a distortional wave polarized along the X_1 axis.
t_2	the specimen transit time for a distortional wave polarized along the X_2 axis.
U_j	the components of the displacement.
U_{j0}	the components of the displacement amplitude of a plane harmonic wave.
V	the velocity of a distortional wave in an isotropic medium.
V_1	the velocity of a distortional wave in a medium of oriented crystallites when the particle motion is parallel to the X_1 axis.
V_2	the velocity of a distortional wave in a medium of oriented crystallites when the particle motion is parallel to the X_2 axis.
$\frac{\Delta V}{V}$	the fractional velocity change associated with the double refraction of a distortional wave propagating in an anisotropic body.
v	the general velocity of a plane wave in an anisotropic body.
\dot{X}_1	the distortional wave velocity when the axis of polarization is parallel to the X_1 axis.
X_2	the distortional wave velocity when the axis of polarization is parallel to the X_2 axis.

Greek Symbols

ζ	the elastic displacement in the X_3 direction.
η	the elastic displacement in the X_2 direction.
ν	the angle between the plane of vibration of a plane polarized wave and the X axis.

- ξ the elastic displacement in the X_1 direction.
- ρ the density of an undeformed elastic medium.
- ψ the phase angle.
- ω the angular frequency.

specify the events that result in a stress-corrosion failure. Stress corrosion may be prevented by reducing or eliminating existing residual tensile stresses that are produced by fabrication or assembly processes. However, this requires a method of measuring these residual stresses.

INTRODUCTION

Figure 1 is a logic diagram that shows the various paths that can be taken to insure that no stress-corrosion failures occur. The four factors required for the initiation of stress corrosion are (1) a susceptible material, (2) a tensile stress, (3) a corrosive environment, and (4) time. Since factors of time and environment are always present during prelaunch checkout, any solution of the stress-corrosion problem must involve the elimination of the susceptible material or the tensile stress. Means have been devised by which certain susceptible alloys can be made resistant to stress corrosion by processes such as coatings and shot peening the surface to produce a compressive residual stress. This approach provides answers for specific alloys but does not constitute a solution of the problem. A real solution will be obtained only when the stress-corrosion mechanism is fully understood. Presently, a visually detected crack is the first evidence of stress corrosion. Research efforts are thus limited

EXPERIMENTAL METHODS FOR DETECTING STRESS CORROSION

Several studies are being conducted to develop methods for detecting the presence of stress corrosion. (1) Internal friction measurements have been made on alloy 7079-T6 to determine whether the internal friction changes when the material is exposed to stress and a corrosive environment. It was found that the energy losses increased with time and also varied with the grain direction. When the stress was removed, the internal friction did not change, and the corrosive environment acting alone had little effect on the damping capacity. Thus the internal friction does change as the stress-corrosion process progresses. (2) Laboratory tests have revealed that the attenuation of ultrasonic surface waves is sensitive to stress-corrosion damage. (3) Acoustic emissions have been detected when aluminum specimens were exposed to stress and a corrosive environment. The emissions were different when only stress was applied, indicating that emissions were produced by changes in the microstructure caused by the stress-corrosion process. (4) The electrical conductivity changes when stressed aluminum specimens are exposed to a corrosive environment, whereas stress or early stages of corrosion alone have little effect on electrical conductivity. Higher frequencies caused greater sensitivity to changes. No changes were observed from applying compressive stresses. These four areas of investigation are concerned with the detection of stress corrosion.

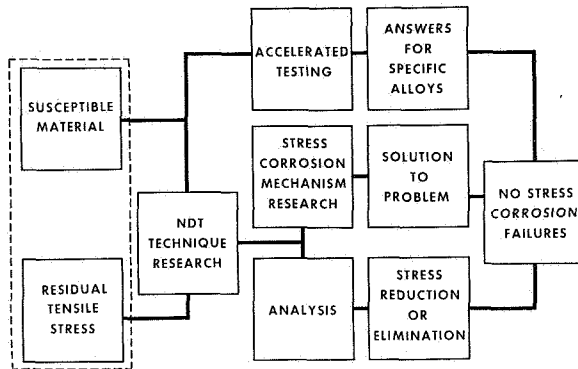


FIGURE 1. APPROACH TO STRESS-CORROSION PROBLEM

because the initiation and process for the occurrence of a microscopic crack cannot be determined. Non-destructive testing techniques must be developed to

Efforts to date for the analysis of residual stress have primarily been devoted to studying the effect of stress on ultrasonic surface and shear wave velocities. Table I gives the acoustic velocity data obtained for surface and shear waves in 2024-T351, 6061-T651, and 7075-T651 aluminum alloys. There is a considerable difference in delay or transit time (which is directly proportional to velocity) when the materials are subjected to stresses of 7×10^6 N/m² (1000 psi) and the yield stress.

TABLE I. ACOUSTIC VELOCITY DATA*

Characteristic	Alloy			
	2024	6061	7075	
Temper	T351	T651-T6	T651	
Modulus N/m ² (lb/in. ²)	7.3 × 10 ¹⁰ (10.6 × 10 ⁶)	7.0 × 10 ¹⁰ (10 ⁷)	7.2 × 10 ¹⁰ (10.4 × 10 ⁶)	
Yield N/m ² (lb/in. ²)	3.3 × 10 ⁸ (47 × 10 ³)	2.8 × 10 ⁸ (40 × 10 ³)	5.0 × 10 ⁸ (73 × 10 ³)	
Delay Time for 2.54 cm (1 in.) Path Length at 7 × 10 ⁶ N/m ² (10 ³ psi), Strain Corrected	1.93 nsec 1.04	3.32 nsec 0.556	3.61 nsec 0.239	(Shear Wave) (Surface Wave)
Delay Time at Yield for 2.54 cm (1 in.) Path Length (nsec)	90.8 48.8	133 22.2	263 17.5	(Shear Wave) (Surface Wave)
Absolute Velocity Shear Wave (m/sec)	3300	3045	3480	
Absolute Velocity Surface Wave (m/sec)	3030	2905	3030	

* Measurements were made at 7 MHz with the exception of Surface Wave Data for 7075 which were made at 5 MHz.

STRESS ANALYSIS

Perhaps the most promising technique being investigated for the analysis of stress is that based on the birefringence of ultrasonic shear waves. Figure 2 is a schematic representation showing the result of a shear wave propagating through an anisotropic material (in this case the anisotropy is caused by the applied stress). If the wave is polarized parallel to the direction of the applied stress (that is, if the particle motion is parallel to the stress direction), the wave will propagate through the material with one velocity, whereas, if it is polarized perpendicular to the stress it will have a different velocity. For any other polarization, birefringence will occur and the wave will be resolved into two components, one traveling parallel and the other perpendicular to the stress direction, with the resultant particle motion as shown. The phase difference between the two components can be used to determine the degree of anisotropy of the material, which in this case is assumed to be caused by stress. Figure 3 is a graph of data that were obtained for 6061-T6 aluminum that had been cold rolled by various amounts.

Birefringence is given in terms of the fractional velocity difference $\Delta V/V$ which is merely the difference between the velocities of the two wave components divided by the average velocity in an isotropic medium. The cold rolling did not change the slope of the stress-birefringence curve but only affected the initial value of the birefringence. The data presented are in agreement with the theory of stress-induced birefringence based on non-linear elasticity theory. One of the complications of this method of stress analysis is that the anisotropy which causes the birefringence can be caused by sources other than stress. In cold rolled material, the other principal source of anisotropy is preferred grain or crystallite orientation. Figure 4 illustrates crystallite preferred orientation. Shown are crystallites randomly oriented, and some that have a particular crystallographic direction aligned parallel to the rolling direction and a specific plane aligned parallel to the rolling plane. Figure 5 illustrates a shear wave propagating through a specimen having preferred grain orientation. One wave component is propagating through the material with a velocity \bar{X}_1 parallel to the rolling direction and the other wave component traveling parallel to the long transverse direction

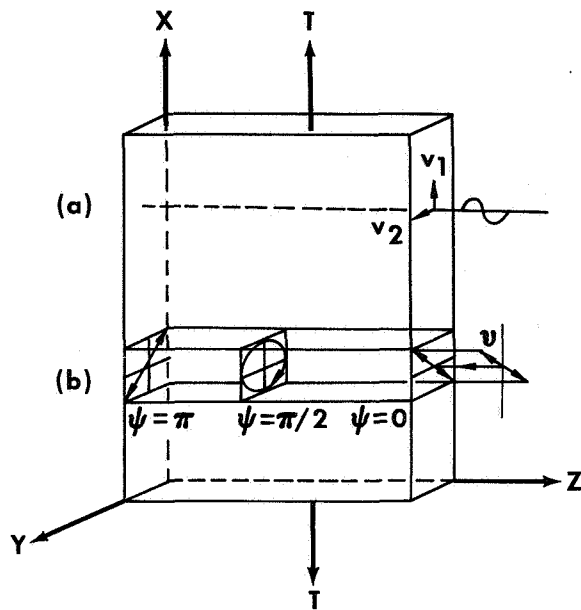


FIGURE 2. (a) DISTORTIONAL WAVE PROPAGATION IN AN ANISOTROPIC MEDIUM AND (b) THE RESULTING PARTICLE MOTION

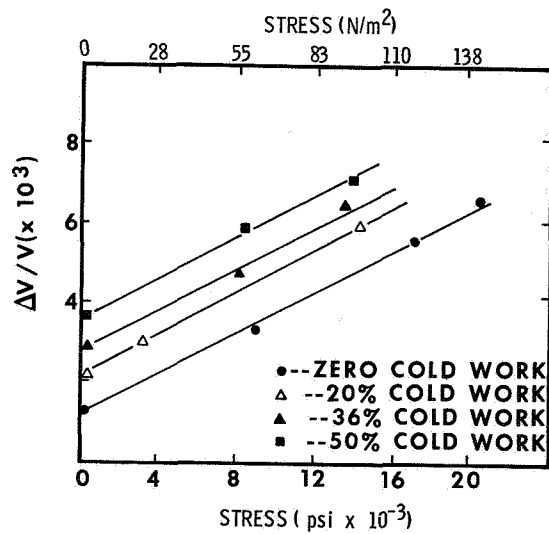


FIGURE 3. STRESS-INDUCED BIREFRINGENCE IN COLD-WORKED 6061-T6 ALUMINUM

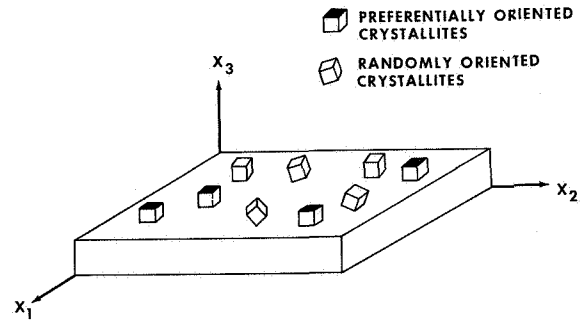


FIGURE 4. CRYSTALLITE PREFERRED ORIENTATION IN A SHEET OF ROLLED METAL

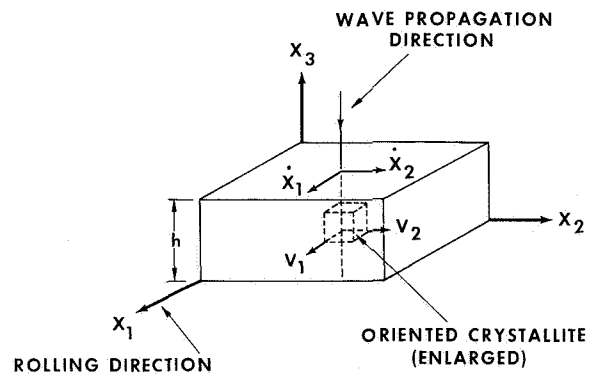


FIGURE 5. WAVE BIREFRINGENCE CAUSED BY PREFERRED ORIENTATION IN ROLLED METAL SHEET

with a velocity \dot{x}_2 . When the waves reach the oriented crystallite, the velocities of propagation (V_1 and V_2) will depend on the particular orientation possessed by the crystallite. If it is assumed that the path length in the oriented crystallites is proportional to the number of oriented crystallites, the shear wave transit times are

$$t_1 = h(1 - F)/V + hF/V_1$$

and

$$t_2 = h(1 - F)/V + hF/V_2$$

whose difference is

$$t_1 - t_2 = hF(V_2 - V_1)/V_1 V_2$$

The above relationship in terms of velocity is

$$(h/X_1 - h/X_2) = \frac{hF(V_2 - V_1)}{V_1 V_2}$$

and

$$\frac{X_2 - X_1}{X_1 X_2} = \frac{F(V_2 - V_1)}{V_1 V_2}$$

If

$$X_2 - X_1 = \Delta V \text{ and } X_1 X_2 \cong V^2,$$

then

$$\Delta V/V(\rho) = VF(V_2 - V_1)/V_1 V_2.$$

The results of this analysis show that, theoretically, the birefringence is a function of the fraction of the crystallites possessing a preferred orientation and the velocities V_1 and V_2 of the waves in the oriented crystallites. To determine the magnitude of this effect, specimens of aluminum were cold rolled to various degrees and the birefringence was measured. X-ray diffraction pole figures were then obtained from which the degree and type of orientation could be obtained. Figure 6 illustrates the pole figure that was obtained for 6061-T6 aluminum cold rolled 50%. The type of

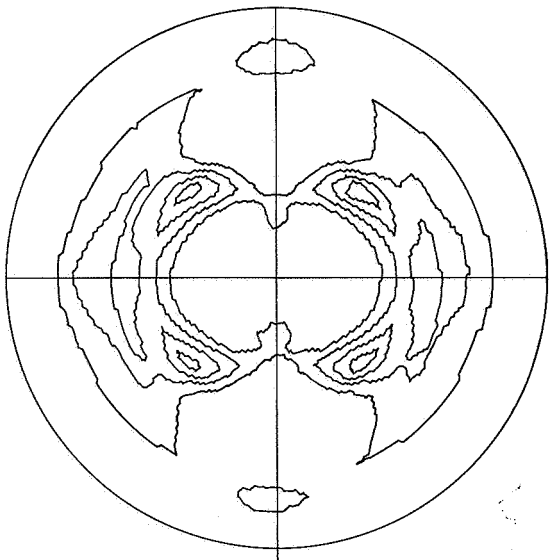


FIGURE 6. ALUMINUM (111) POLE FIGURE

orientation indicated by this pole figure is illustrated in Figure 7. Thus, the orientation is known but the

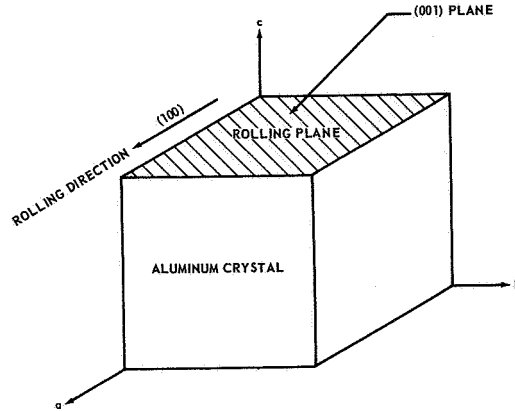


FIGURE 7. BASIC ORIENTATION PRODUCED IN COLD-ROLLED 6061-T6 ALUMINUM

wave velocities for an aluminum crystallite with this orientation have to be known in order to calculate the birefringence resulting from the preferred orientation. Figure 8 shows the general state of stress for a crystal. By using this general stress condition, the following list of equations of motion for wave propagation in anisotropic media can be obtained.

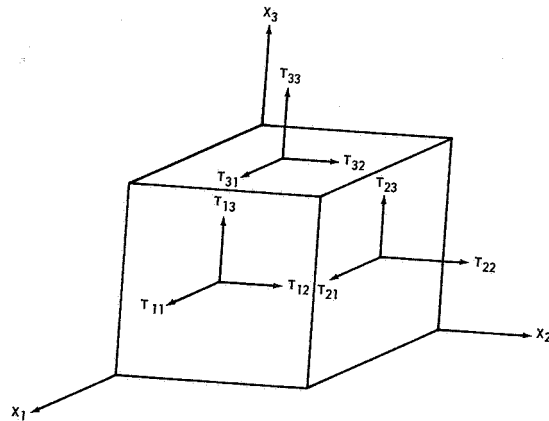


FIGURE 8. THE COMPONENTS OF STRESS FOR A RECTANGULAR CARTESIAN COORDINATE SYSTEM

$$\rho \ddot{\xi} = \frac{\partial T_{11}}{\partial X_1} + \frac{\partial T_{21}}{\partial X_2} + \frac{\partial T_{31}}{\partial X_3} ,$$

$$\rho \ddot{\eta} = \frac{\partial T_{12}}{\partial X_1} + \frac{\partial T_{22}}{\partial X_2} + \frac{\partial T_{32}}{\partial X_3} ,$$

$$\rho \ddot{\zeta} = \frac{\partial T_{13}}{\partial X_1} + \frac{\partial T_{23}}{\partial X_2} + \frac{\partial T_{33}}{\partial X_3} .$$

Tensor representation of the above equations is

$$\rho \ddot{U}_j = \frac{\partial T_{ij}}{\partial X_i}; \quad i, j = 1, 2, 3.$$

Generalized Hooke's Law in tensor form is

$$T_{ij} = c_{ijkl} e_{kl} .$$

Strain - displacement relationship in tensor form is

$$e_{kl} = 1/2 \left[\frac{\partial U_k}{\partial X_l} + \frac{\partial U_l}{\partial X_k} \right]$$

and assume the case of a plane harmonic wave propagating through the medium is given by

$$U_j = U_{j0} \exp [i(\omega t - K l_n X_n)]; \quad j, n = 1, 2, 3$$

where $K = \frac{\omega}{v}$ and l_n are the direction cosines of the normal to the wavefront.

By applying the generalized relationship for Hooke's law and the strain-displacement relationship and assuming the case of a plane wave, the following three equations involving the wave velocity can be obtained from the previous list of equations for wave propagation.

$$\rho v^2 U_1 = D_{11} U_1 + D_{12} U_2 + D_{13} U_3$$

$$\rho v^2 U_2 = D_{12} U_1 + D_{22} U_2 + D_{23} U_3$$

$$\rho v^2 U_3 = D_{13} U_1 + D_{23} U_2 + D_{33} U_3$$

where

$$D_{11} = c_{11} l_1^2 + c_{66} l_2^2 + c_{55} l_3^2 + 2 c_{16} l_1 l_2 + 2 c_{56} l_2 l_3 + 2 c_{15} l_1 l_3 .$$

$$D_{12} = c_{16} l_1^2 + c_{26} l_2^2 + c_{45} l_3^2 + (c_{12} + c_{66}) l_1 l_2 + (c_{25} + c_{46}) l_2 l_3 + (c_{14} + c_{56}) l_1 l_3 .$$

$$D_{13} = c_{15} l_1^2 + c_{46} l_2^2 + c_{35} l_3^2 + (c_{14} + c_{56}) l_1 l_2 + (c_{36} + c_{45}) l_2 l_3 + (c_{13} + c_{55}) l_1 l_3 .$$

$$D_{22} = c_{66} l_1^2 + c_{22} l_2^2 + c_{44} l_3^2 + 2 c_{26} l_1 l_2 + 2 c_{24} l_2 l_3 + 2 c_{46} l_1 l_3 .$$

$$D_{33} = c_{55} l_1^2 + c_{44} l_2^2 + c_{33} l_3^2 + 2 c_{45} l_1 l_2 + 2 c_{34} l_2 l_3 + 2 c_{35} l_1 l_3 .$$

$$D_{23} = c_{56} l_1^2 + c_{24} l_2^2 + c_{34} l_3^2 + (c_{25} + c_{46}) l_1 l_2 + (c_{23} + c_{44}) l_2 l_3 + (c_{36} + c_{45}) l_1 l_3 .$$

The D_{ij} coefficients are functions of the direction cosines of the normal to the wavefront and the elastic constants of the material. The condition that these three homogeneous equations have a non-vanishing solution is that the following determinant be zero.

$$\begin{vmatrix} (D_{11} - \rho v^2) & D_{12} & D_{13} \\ D_{12} & (D_{22} - \rho v^2) & D_{23} \\ D_{13} & D_{23} & (D_{33} - \rho v^2) \end{vmatrix} = 0 .$$

Since aluminum has only three non-zero independent elastic constants (C_{11} , C_{12} , and C_{44}), the D_{ij} coefficients for the specific case of aluminum become

$$D_{11} = c_{11} l_1^2, \quad D_{12} = c_{12} l_1 l_2, \quad D_{13} = 0 .$$

$$D_{22} = c_{44} l_3^2, \quad D_{23} = c_{44} l_2 l_3, \quad D_{33} = c_{44} l_2^2 .$$

Thus, the determinant simplifies to

$$\begin{vmatrix} (D_{11} - \rho v^2) & D_{12} & 0 \\ D_{12} & (D_{22} - \rho v^2) & D_{23} \\ 0 & D_{23} & (D_{33} - \rho v^2) \end{vmatrix} = 0 .$$

If the D_{ij} coefficients are calculated for the specific orientation shown previously, the two velocities are the same. Thus the birefringence is zero, theoretically. The result indicates that the experimentally determined birefringence is caused entirely by stress.

CONCLUSION

Research is progressing toward a solution for the non-destructive measurement and analysis of stress corrosion and residual stress. Experimental methods to detect stress corrosion are by (1) internal

friction, (2) electrical conductivity, (3) surface wave attenuation, and (4) acoustic emission. Experimental methods to analyze residual stress are by (1) surface wave velocity changes, (2) shear wave velocity changes, and (3) shear wave birefringence. Any successful technique will be of tremendous value in eliminating stress-corrosion failures.



MATERIAL DESIGNS FOR ELECTRONIC APPLICATIONS

By

Eugene C. McKannan and James E. Curry

SUMMARY

1. Motor Brushes. The development of new materials for fabrication of dc motor brushes is discussed. The need for brush materials having good electrical and lubricating properties while operating in a vacuum environment required evaluation of numerous materials. A discussion follows of the wear process as affected by velocity, current density, material fabrication and initial operation. The evaluation of complete motor assemblies emphasizes high contact efficiency, high temperature resistance, and low noise level.

2. Dielectrics for Wire Coatings. A comparison is made of the use of a thin polyimide coating versus a teflon coating for insulating wires in cryogenic environments. The mechanical and electrical properties of both wire insulation materials are presented.

3. Electrical Properties of Cryogenic Fluids. The breakdown voltage (strength) of several liquid cryogens was determined. The gaseous and liquid breakdown strengths of three cryogens are compared. A theory for the breakdown strengths of the liquid cryogens was formulated and contributes an important link in the basic theory of electrical discharge.

4. Potting Compounds. The protection of electronic circuitry by potting compounds and coating resins is discussed. The adhesion, thermal expansion and dielectric properties as affected by chemical stability of the materials are mentioned. The necessity for careful preparation of the protective potting compounds and coatings is explained. The complex materials evolving from experiments in developing potting and coating compounds are provided by combining desirable molecular structures from different polymers and by providing new curing systems.

DC MOTOR BRUSHES

The development of improved electrical brushes was needed to realize the benefits of simple direct current (dc) rotating equipment in the space

environment. Some typical applications for dc motors are (1) the drive motor for the pumps on the hydraulic system, the cooling system, or the life-support system, (2) the deployment and positioning of solar panels and wings, (3) attitude control when using angular momentum in flywheels and torque motors as in the Apollo Telescope Mount, and (4) the high-powered driving and lifting motors in moon-based equipment. Dc motors provide the least complex solution to the problem of converting electrical energy to mechanical energy in space. All the power generating devices produce direct current, and the use of direct rather than alternating current precludes the additional weight and complexity of inverters. Direct current motors also offer the advantages of sensitive control and high torque at low speeds.

Brush motors are simpler than motors in which the field is switched with external high-powered transistors or other electronic commutation methods. However, a materials development was required because standard graphite brushes wore very rapidly in a vacuum environment. The lubricity of graphite depends upon the water vapor or oxygen in the atmosphere rather than upon its own inherent structure. The problem of the rapid wear of graphite brushes in high altitude aircraft was solved by adding metallic halides to the brushes. However, this correction does not work at the very low pressures of orbital altitudes.

A search was initiated for a new material that would be suitable for motor brushes used in space vehicles. Based on the Materials Division's experience with dry film lubricants, crystal structure, and other solid state properties, the following list of materials was selected for testing: disulfides, diselenides, and ditellurides of molybdenum, tungsten, niobium, tantalum, and titanium in combination with the additives of silver, silver sulfide, copper or iron. Table I gives the service life of commercially available graphite and high altitude brushes compared with molybdenum disulfide (MoS_2) and silver (Ag) brushes that have operated so well in vacuum. The best experience to date has been obtained with NbSe_2 and MoS_2 mixtures.

In addition to being dependent upon solid state properties, the brush characteristics also depend

TABLE I. MOTOR BRUSHES AT 2000 rpm IN VACUUM ENVIRONMENT OF 1.33×10^{-6} N/m², 300° K (10^{-8} mm Hg, 80° F)

% Composition	Service Life, Hours	Wear Rate cm/hr (in./hr)	Current Density A/cm ² (A/in ²)
Graphite	6	2.54 (1.0)	0.775 (5)
High Altitude	28	2.54×10^{-2} (10^{-2})	0.775 (5)
90 MoS ₂ - 10 Ag	2080	2.54×10^{-5} (10^{-5})	1.55 (10)
86 MoS ₂ - 14 Ag	5600	2.54×10^{-5} (10^{-5})	1.55 (10)
73 MoS ₂ - 27 Ag	5580	2.54×10^{-6} (10^{-6})	2.64 (17)
60 MoS ₂ - 40 Ag	32	2.54×10^{-3} (10^{-3})	1.86 (12)
100% NbSe ₂	2480+	2.54×10^{-4} (10^{-4})	3.10 (20)
80 NbSe ₂ - 20 MoS ₂	1200+	2.54×10^{-4} (10^{-4})	3.10 (20)

upon preparation conditions because they are formed by compaction of powder. Powder with the smallest attainable particle size (2.5μ) is mixed in measured ratios and placed in a graphite mold. Mold pressure is applied to about 2.41×10^7 N/m² (3500 psi). The temperature is then increased to 1200° K for purposes of sintering. These conditions are held for a few minutes, the pressure is released and the temperature is reduced. A solid piece is produced from which several brushes may then be cut. Anisotropy, or directionality in properties, is introduced because the material compacts with a preferred grain orientation. Therefore, the brushes must be cut so that the laminations in the contact face are perpendicular to the direction of pressing and are parallel to the axis of the commutator shaft. Good brushes must have high conductivity, or conversely, low resistivity, with minimum friction, wear, and noise. Figure 1 illustrates electrical properties of several brush materials. Pure silver is shown for purposes of comparison. NbSe₂ is a good conductor and a moderately good lubricant in vacuum. MoS₂ is a semiconductor whose resistivity curve would be far

off the top of Figure 1 and have an opposite slope to the curves shown. However, its resistivity decreases with the addition of increasing amounts of silver.

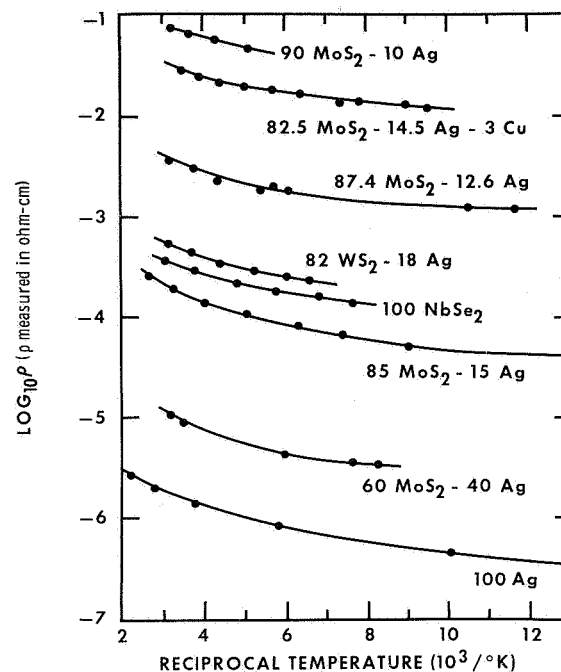


FIGURE 1. RESISTIVITY VS. TEMPERATURE OF BRUSH MATERIALS

The conduction process appears to be a combination of the continuous metallic conduction over very small cross sectional paths, coincident with the conduction of a highly degenerate semiconductor (the host material). The host lattice contains added metallic atoms in sufficient concentration that they interact with each other. When this interaction is sufficiently strong, these atoms form an electronic structure of their own, independent of the host lattice.

The wear process begins with an unstable, transient condition. A film of the brush material must be transferred to the commutator, and the oxide coating on the commutator must be removed in order for stable electrical conduction to proceed. The film formation on the commutator begins immediately but requires several hours to become stable. Figure 2 is a plot of wear rate, contact resistance, and noise level for the run-in or initial instability of a typical brush material. The run-in time is required to establish contact spots on the commutator surface by

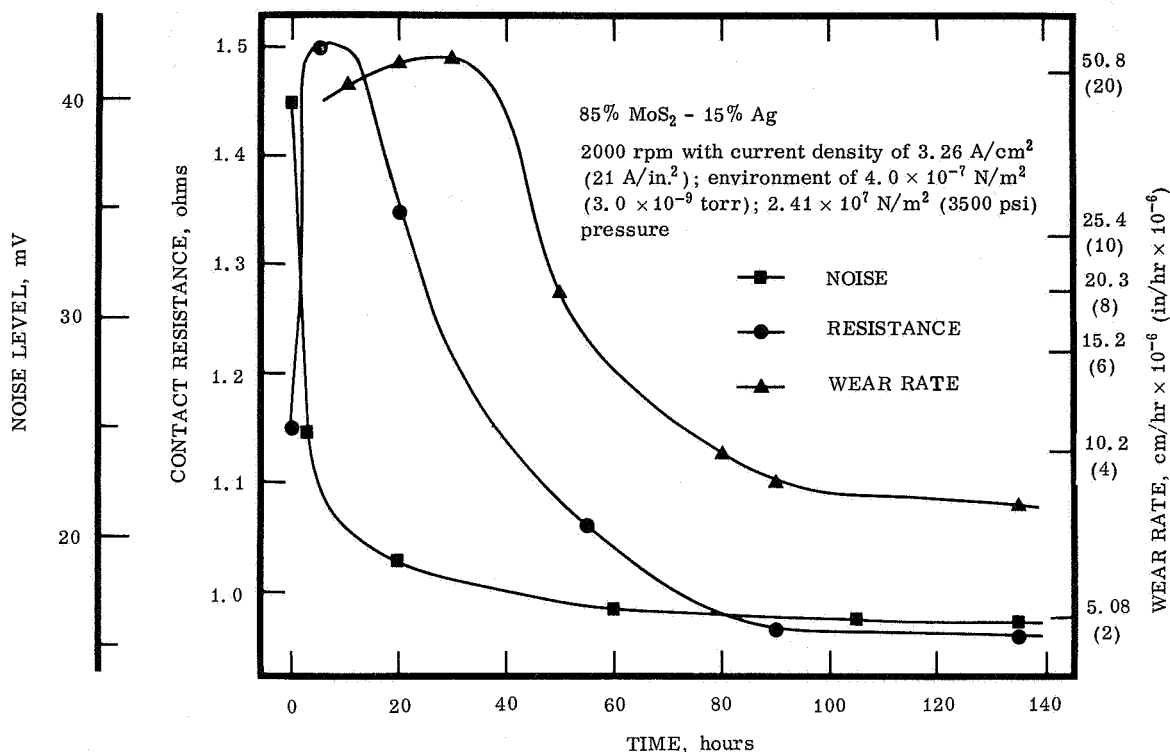


FIGURE 2. RUN-IN PARAMETERS

the process of fretting the oxide coating. The fretting action is required to breakdown and penetrate the copper-oxide layer. The wear rate is dependent upon the surface temperature created during this fretting action.

When examining the effects of wear rate caused by the variation in motor speed (rpm), as the speed is increased the wear rate rises sharply and then stabilizes to a relatively uniform, low value. The contact resistance also increases and then reduces to a steady value over the same period of time. Individual contact points are established on the brush face for each particular speed of rotation, and if the speed is increased, the contact areas are effectively reduced. Additional work or fretting the copper oxide is required to establish a larger contact area, and until this occurs, surface temperature increases with a resulting increase in the brush wear rate. Figure 3 shows the dependence of rotational speed on the stable wear rate. Material pressed at 2.41×10^7 N/m² (3500 psi) is harder than that pressed at 2.1×10^7 N/m² (3000 psi) and thus produces the more stable wear characteristics. Results on materials pressed at even higher pressures indicated no further improvement. These results

indicate that the lubricating film is very stable for long periods of time in vacuum once the initial run-in is accomplished.

Wear rate also is dependent on the current density through the brush (Fig. 4). The wear rate decreases rapidly as the film is transferred to the commutator in the same manner as the wear rate depended on the rotational speed. When the current density is increased, the wear rate increases because of the heating effect and reduced contact surface. At the higher current density the wear rate will stabilize at a greatly reduced value after the initial run-in. At some value in current density the temperature in the interface appears to be high enough to soften the destructive particles and the wear rate decreases.

Apparently when arcing occurred, caused by brush bounce from discontinuities in film transfer, the metallic element such as silver agglomerates near the contact interface and separates from the host material (MoS₂) because of differential thermal expansion. Although useful for long periods of time, the MoS₂-metallic brushes were troublesome once high temperature arcing was initiated. The arcing problem with silver (Ag) led to increased emphasis on the highly conductive niobium diselenide.

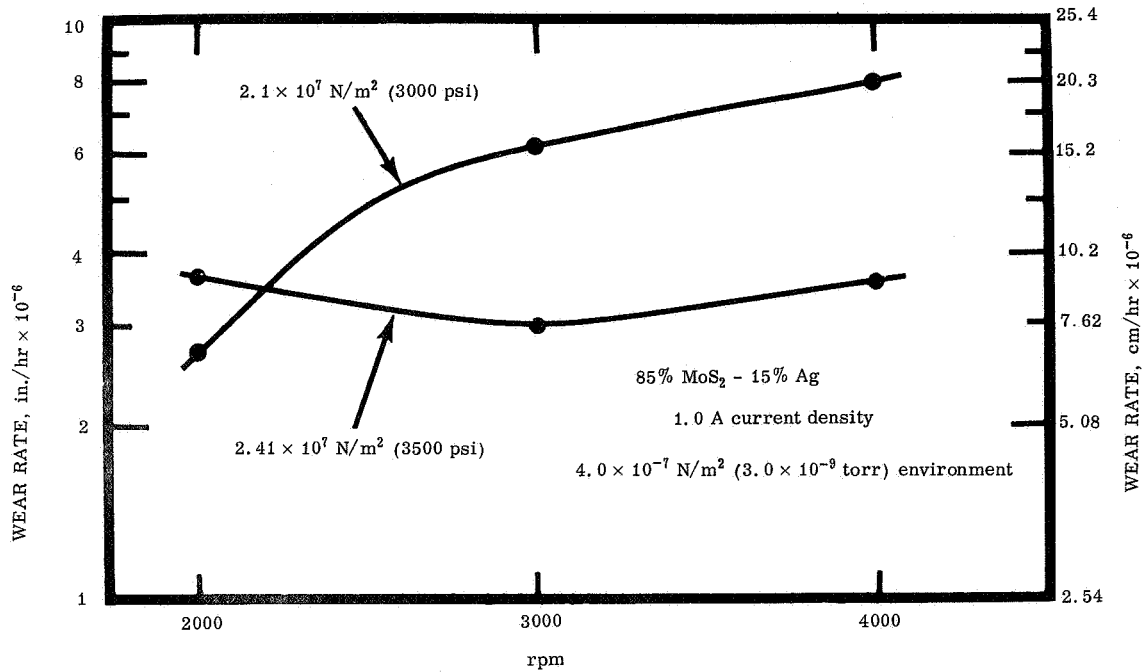


FIGURE 3. WEAR RATE VS. VELOCITY

Noise measurements were made to provide additional information about the run-in process. Figure 5 shows two oscilloscope traces. In each case the

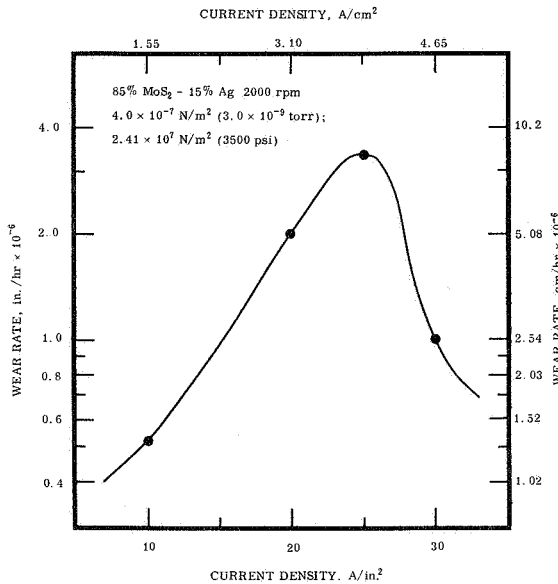


FIGURE 4. WEAR RATE VS. CURRENT

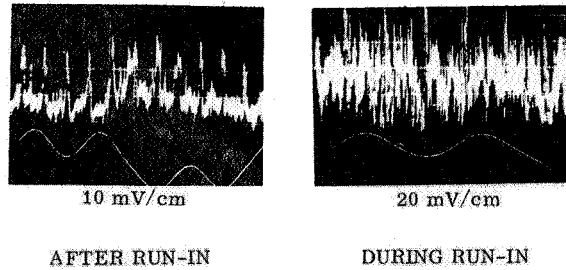


FIGURE 5. BRUSH NOISE

lower curve is a trigger-wave form derived from the driving magnets. A high noise level and the purely random nature of noise during run-in are evident in the trace that was obtained during the first hour of running. This is a characteristic of the fretting process. The rms value of the noise is greater than 60 mV. Except for the periodic spike as the brush trailing edge leaves each segment of the commutator

and collapses its magnetic field, the low random noise is shown after run-in. The periodic spike is approximately 25 mV and the general noise level is less than 10 mV. These traces indicate that the developed brushes are less noisy in vacuum than are typical carbon brushes when operating in air.

The final proof for the brush or other motor material has been the evaluation of complete motors. Table II lists the results from many successful motor-generator tests. Over 1500 hours of intermittent operations have been accumulated on one

TABLE II. DC MOTOR GENERATOR EVALUATIONS IN ENVIRONMENT OF 1.33×10^{-4} N/m² (10^{-6} mm Hg)

Ambient Temperature, °K	97	294	423	503
Shaft Temperature, °K	288	433	471	508
Input Power, W	85	190	183	220
Motor Efficiency, %	52	49	49	49
Velocity, rpm	700	600	580	615
Torque, N-m (in.-lbs)	1.02 (9)	1.36 (12)	1.58 (14)	1.58 (14)
Brush	MoS ₂ /Ag		NbSe ₂ /MoS ₂	

motor-generator set. This set has been operated at ambient conditions from 77°K (-196°C) to over 503°K (+230°C) in an environment at 1.33×10^{-4} N/m² (10^{-6} mm Hg). The most recent tests have involved brushes of MoS₂ and NbSe₂. These brushes have provided high contact efficiency, high temperature resistance, and low noise. Concurrent programs on bearings and on electrical insulation for use in motors and in other applications in space have provided the other critical elements of the successful motors. However, the most critical component of the dc motor operating in vacuum is the brush.

The experience of the Materials Division indicates that all of the materials are available to design, build, and operate motors in the space environment for long periods of time at reasonably high loads.

DIELECTRICS FOR WIRE COATING

Teflon (TFE) is almost universally used throughout the Saturn vehicle and in other space applications. It is an extremely satisfactory wire coating except for its lack of flexibility in the cryogenic environment. Cabling is routed through a liquid hydrogen tank to provide voltage to liquid level sensors, to thermocouple temperature sensors, or to electrodes for electro-phoretic control of the liquid hydrogen surface in zero gravity. When equipment is operated on the moon's surface, the same cold temperature conditions will prevail during the lunar night. Hence, several probable insulation schemes were evaluated to provide a flexible wire coating for a cryogenic environment. Most of the polymeric materials available for such wire coatings have a glassy transition temperature which makes them extremely stiff and brittle at cold temperatures. But one of the means by which a cold temperature flexible coating may be obtained is to use a material which has very little change in its elastic properties with temperature. High temperature resistant insulations provide a first clue. A very thin coating will serve as a cold temperature flexible material if the thin coating will provide the mechanical toughness and the electrical insulation required. A thin coating undergoes much less stress in bending than a thicker coating.

The following list of materials was considered for wire coatings for cryogenic service: (1) enamels - polyvinyl formal, polyester, polyamide, aluminum phosphate, polyimide; (2) extrusions - polyvinyl chloride, polytetrafluoroethylene; (3) fibers - glass, asbestos, polyester. The polyimide coating provided the greatest mechanical protection in addition to completely adequate insulation in a very thin film 38 μ (1.5 mils) thick as compared to the typical Teflon insulation of 280 μ thickness (11 mils). In addition, the thin-film polyimide insulation is LOX compatible and could reduce the mass of each Saturn V stage by 136 kg (300 lbs) considering the 45 700 m (150 000 ft) of insulated conductors in each stage. Table III gives some mechanical properties of the polyimide thin coating as compared to the thicker coating of Teflon used in the standard wire construction. The relative flexibility is indicated by the size of the mandrel around which a wire can be bent at any given temperature. While these wires are equally flexible at room temperature, the Teflon wire requires 10 times the diameter at cryogenic temperatures to avoid cracking. This is a standard flexibility

TABLE III. MECHANICAL WIRE COATING PROPERTIES

	Polyimide	TFE
●Coating Thickness, μ (mils)		
	35.6 (1.4)	280 (11.0)
●Flexibility, Minimum Diameter Bend, cm (in.)		
296° K	0.163 (0.064)	0.163 (0.064)
213° K	0.318 (0.125)	0.318 (0.125)
77° K	0.318 (0.125)	3.18 (1.250)
4° K	0.318 (0.125)	3.18 (1.250)
●Compression Cut-through, Breakdown (kV)		
After 48 Hours Under 98 N force (22 lbf)		
77° K	9.0	25.0
296° K	13.9	15.0
393° K	14.0	Short
523° K	11.5	Short

test used throughout the wire and cable industry. In addition, scraping, tearing, or cutting when pressed against a sharp edge or point is an important mechanical property. The data show that when these wires are given a standard cut-through test, the Teflon relaxes and allows the conductor to be shorted, whereas the tougher polyimide coating continues to provide protection.

The dielectric constant of the polyimide material is slightly greater than that of Teflon (Table IV), and the increase in the capacitance between wires will increase the cross talk. This property is controlled by spacing and twisting the wire. The dissipation factor is slightly higher for the polyimide material, but is entirely acceptable in most signal wire applications. The surface and volume resistivities are quite similar for both coatings in vacuum or in liquid cryogenics.

One of the most common tests used to compare wire insulations after any given environmental exposure is the dielectric breakdown or high voltage sparkover. Table IV compares 280 μ thickness (11 mils) of Teflon to 35.6 μ thickness (1½ mils) of polyimide, with breakdown voltages in kilovolts. Since a breakdown strength of 8 kV is satisfactory for most space vehicle applications, the safety factor for either material is large. The thickness of the

TABLE IV. ELECTRICAL WIRE COATING PROPERTIES

	Polyimide	TFE
●Dielectric Constant	3.0	2.0
●Dissipation Factor	0.0009	0.0003
●Resistivity, ohms		
After 15 Days at 353° K and 95% RH		
Surface	2×10^{13}	2×10^{13}
Volume	7×10^{12}	2×10^{13}
●Breakdown Voltage, (kV)		
296° K Air	13	19
213° K Air	12	19
77° K LN ₂	9	19
20° K LH ₂	9	17
4° K LHe	8	17
523° K Air	8	16
After 120 Days at 393° K		
in Air	13	17
in Vacuum	16	19
After 15 Days at 353° K and 95% RH		
	12	18

Teflon insulation is generally not required for breakdown strength or any other electrical properties, but rather to provide a large safety factor for the mechanical properties such as cut-through or scrape resistance. With such a tough insulation as the polyimide material, the extra safety factor in thickness is not required.

ELECTRICAL PROPERTIES OF CRYOGENIC FLUIDS

When any wire coating mechanically splits or cracks during a breakdown test, it will not necessarily breakdown electrically unless enough moisture and dirt are present for a discharge path. When the cracking occurs in air the discharge path is always present, but when the cracking occurs in LN₂ or LH₂ or LHe, the fluid is a sufficiently clean dielectric to help insulate the conductor. The fluid does not provide mechanical separation, however. A literature search indicated that no data were available on the breakdown strength of liquid hydrogen. Previously,

researchers in this field used hydrocarbons like transformer oils rather than liquid hydrogen. The breakdown strength of liquid hydrogen was needed because of its importance in and around wire coatings (in filling cracks and in permeating into the insulation), and in electrophoretic control of LH_2 in zero gravity.

Figure 6 graphs the breakdown voltage versus spacing of 1.27-cm diameter ($\frac{1}{2}$ -in. diameter) spheres in 3 cryogenics: liquid hydrogen, liquid nitrogen, and liquid helium. Past experience with

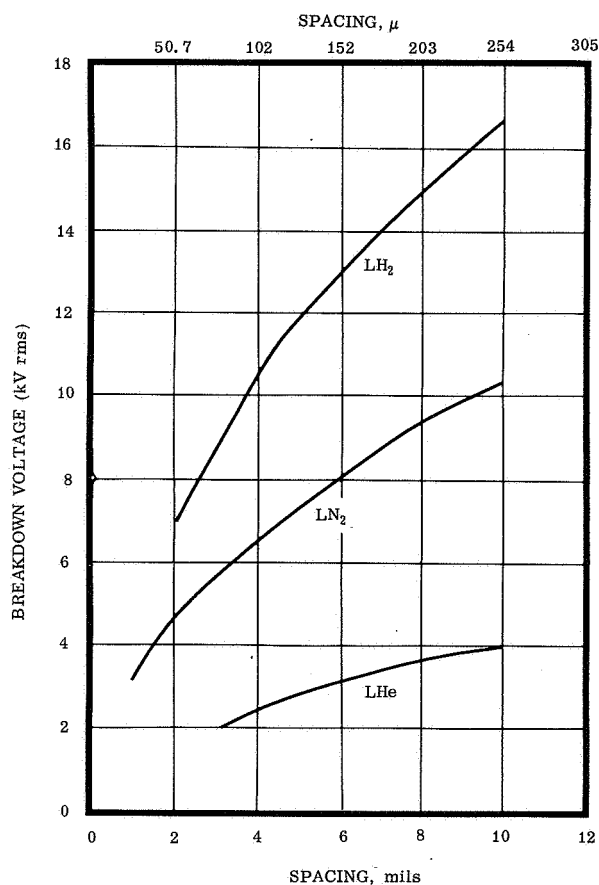


FIGURE 6. 60 Hz BREAKDOWN IN CRYOGENS

gasses had not indicated that liquid hydrogen had such a high breakdown strength. Figure 7 indicates the breakdown strength of gaseous nitrogen, gaseous hydrogen, and gaseous helium. These data correlate with the Townsend discharge process for gases, which is dependent on the kinetic mean free path. In the liquid, however, the positions of the hydrogen and nitrogen were reversed. This was difficult to

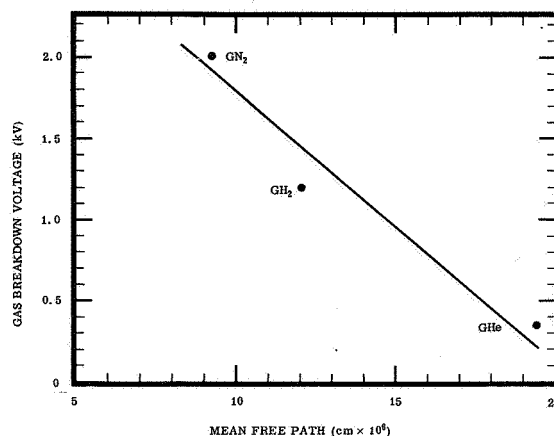


FIGURE 7. GASEOUS BREAKDOWN

explain until it was realized that a different process would prevail in the liquid. Breakdown theory is well described for gases by Townsend and for regular solids by energy band theory, but a good theory for the breakdown strength of liquids did not exist. These experimental data suggested that the inter-atomic spacing of the atoms in the liquid might be a controlling factor, and as shown in Figure 8, the liquid hydrogen breakdown strength can be explained in this

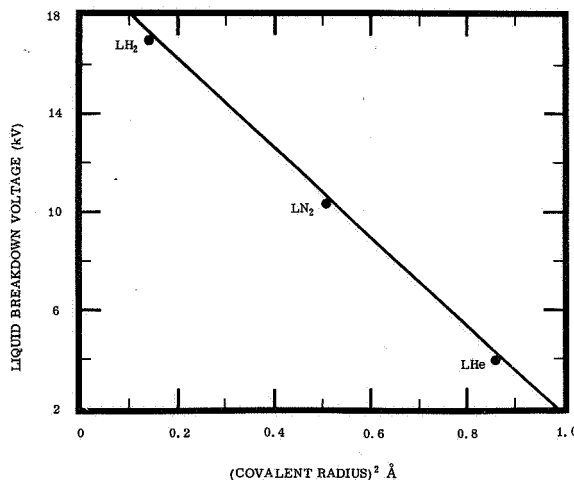


FIGURE 8. LIQUID BREAKDOWN

manner. Physically, the covalent radius in a liquid has much the same effect on ionization as the mean free path in a gas. Therefore, the covalent radius

gives an indication of the theoretical mechanism of breakdown strength in liquids and provides a modification to Townsend's theory to make it applicable to liquids. The results of this work make an important contribution to the basic theory of electrical discharge.

One problem arose when it was determined that a bubble was formed with each discharge. If the bubble occurred first, it would initiate a typical gas discharge. However, all observations led to the conclusion that the bubble was the result of energy dissipation after the discharge because a test was made well below the boiling point where no nucleate boiling bubbles were present and because the observed bubbles never spanned the entire distance between electrodes. At least some liquid was always involved in the discharge.

The knowledge of the breakdown strength of liquid hydrogen makes the electrophoretic control of liquid hydrogen surfaces in zero gravity much more feasible than in other cryogenic liquids. From the safety point of view, an electrostatic discharge which might by chance occur in liquid hydrogen is not as dangerous as it previously might have been considered.

POTTING COMPOUNDS

The requirements for casting and coating resins for the protective encapsulation of electronic circuitry fall into two categories depending upon the nature of the electronics. For cordwood modules where the circuit elements are stacked in a three dimensional array (Fig. 9), a potting compound or filled resin that can be poured around the components is normally used. This resin cures or hardens under conditions that must not be detrimental to the components. It serves to mechanically ruggedize the assembly and provides the dielectric environment for the circuitry. The other category (Fig. 10) is a conformal coating which is normally applied to printed circuit boards for some of the same reasons. A conformal coating must cure to an elastomeric or rubbery solid, while potting compounds cure to a more rigid solid. A sampling of the most critical requirements that must be met by each type of material is listed in Table V.

There are no known commercial products in either category which satisfy all of these requirements. Some of the requirements are quite contradictory; for example, good polymer dielectrics are not generally good adhesives. Yet, good

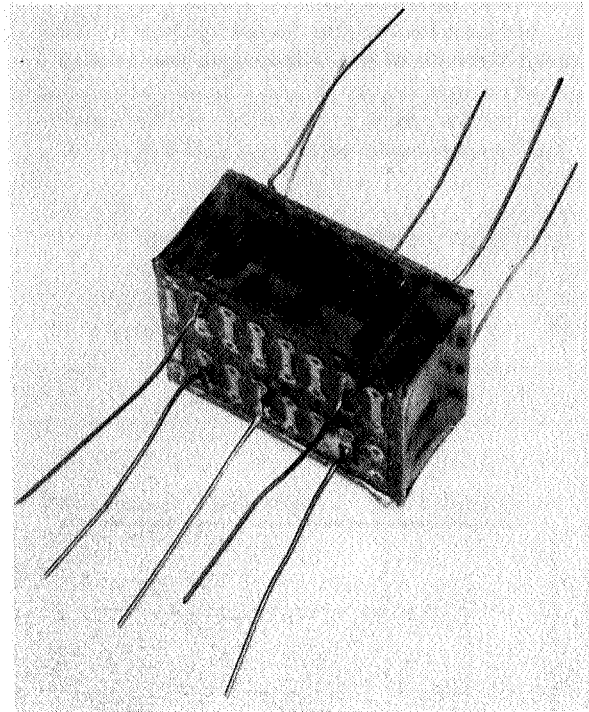


FIGURE 9. CORDWOOD MODULE IN POTTING COMPOUND

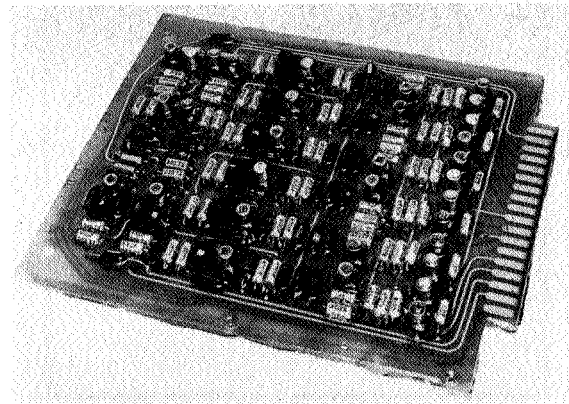


FIGURE 10. PRINTED CIRCUIT BOARD WITH CONFORMAL COATING

adhesion to a variety of substrates is an obvious requirement of both potting compounds and conformal coatings. It is essential that the potting compound's linear coefficient of thermal expansion approach that of the circuitry materials. So far, this has been impossible without the addition of inorganic powders or fillers to the resins. Organic polymers

TABLE V. REQUIRED PROPERTIES FOR POTTING COMPOUNDS AND CONFORMAL COATINGS

<u>Property</u>	<u>Potting Material</u>	<u>Conformal Coating</u>
Coefficient of linear thermal expansion	$10-20 \times 10^{-6}$ in/in $-^{\circ}\text{C}$ maximum	--
Dielectric constant (1 kHz)	3.0 maximum	3.0 maximum
Dissipation factor (1 kHz)	0.01 maximum	0.01 maximum
Volume resistivity	10^{14} ohm-cm minimum	10^{14} ohm-cm minimum
Outgassing potential	100 micromoles max./100 gms. resin after 500 hours/ 150°C / 1.33×10^{-3} N/m ² (10^{-5} torr)	Same
Water absorption	0.5% maximum	0.5% maximum
Adhesion, N/m ² (psi)	0.35×10^7 (500)	0.35×10^7 (500)
Sterilization tolerance		
(1) Dry heat	withstand 135°C for 24 hours	Same
(2) Ethylene oxide	withstand EtO environment of 500 ± 50 mg/liter atmosphere for 24 hours @ 24°C and 35% RH	Same

inherently have much higher coefficients of thermal expansion than are desired for electronic uses.

Prolonged chemical and thermal stability is essential for several reasons in addition to the requirement for sterilization. Degradation of the polymer can adversely affect its dielectric properties. The outgassing products evolved during thermal degradation can contaminate life support systems and optical surfaces.

The Materials Division is working to develop improved potting and conformal coating resins.

The generic classes of resins, e. g., silicones, epoxies, or polyurethanes, contain certain individual combinations having the necessary properties. Through molecular architecture the linkages and substituents that confer desirable properties on individual polymer classes can be incorporated into a single molecular chain.

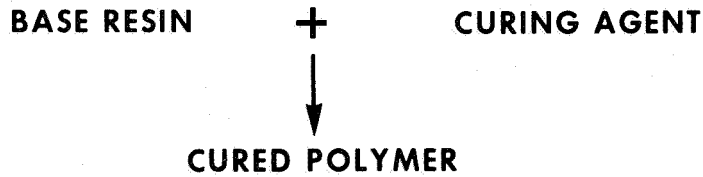
A curing agent or catalyst (Fig. 11) must be added to the base resin to harden it into a useful encapsulant. Amines, which are organic derivatives of ammonia, are popular curing agents for epoxies. Limited experimentation with novel amine curing agents indicates that they can bring commercial epoxies closer in line with present requirements. Some epoxies cured with *n*-methylaniline-formaldehyde adducts developed under this program have dielectric constants that vary less than 0.1 unit over the temperature range from 25 to 150°C . Simultaneous optimization of curing agent, base resin and other additives are required for a good epoxy resin.

As for the base resin problem, epoxies and silicones individually have complementary desirable traits and some individual disadvantages. Figure 12 shows a polymer structure prepared during our program that structurally incorporates certain linkages common to both epoxies and silicones, which are identified in the formula. This polymer is a result of both polymer systems and combines some properties of each. The properties tabulated in Figure 12 show the success in meeting some of the requirements.

The examination of any highly complex material of this type is always subject to our ability to prepare it. In this case, virtually none of the starting intermediates were available commercially and some had never been reported in chemical literature. To complicate matters, a polymer of the above structure cannot be formed by conventional processes of epoxy chemistry, and more than ten individual synthetic steps are needed for its preparation by the process now used. Other approaches are being investigated to improve this situation.

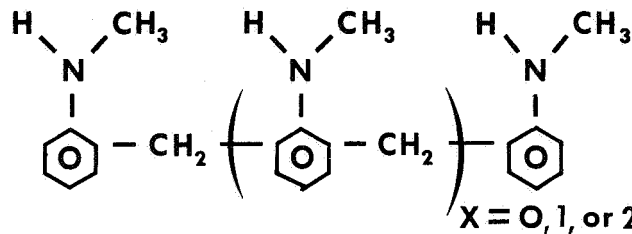
Similar logic has led to studying urethane-silazane polymers shown in Figure 13. This polymer should have a lower dielectric constant and improved thermal stability. There may be a hydrolytic stability problem with the silazane linkage, but the magnitude of this effect cannot be evaluated quantitatively until the actual polymer is evaluated. The synthesis program has progressed to a point that urethane-silazane structures can be prepared.

The basic approach to potting compounds has been solved. Combining the functionality



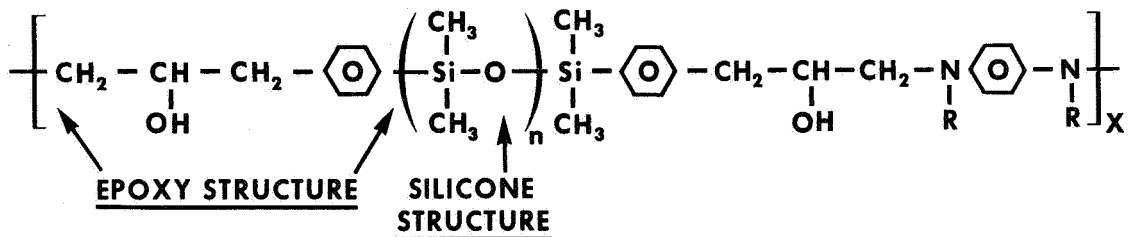
GENERALLY IMPARTS LOWER DIELECTRIC CONSTANT
THAN CONVENTIONAL ORGANIC AMINE CURATIVES.

B. AMINE - FORMALDEHYDE ADDUCTS



LOWERS TEMPERATURE DEPENDENCE OF DIELECTRIC CONSTANT

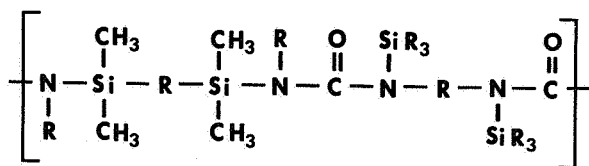
FIGURE 11. NOVEL CURING AGENTS FOR CONVENTIONAL EPOXIES



PHYSICAL FORM RANGES FROM ELASTOMERIC
TO RIGID SOLID DEPENDING UPON VALUE OF n

KEY PROPERTIES	EPOXY - SILICONE	TARGET VALUES
DIELECTRIC CONSTANT AT 1 kC	2.4 AT 25°C 2.8 AT 150°C	3.0 MAXIMUM
DISSIPATION FACTOR AT 1 kC AND 25°C	0.008	0.01 MAXIMUM
VOLUME RESISTIVITY ohm-cm	7×10^{13}	10^{14} AT 25°C MINIMUM 10^{10} AT 100°C
ETHYLENE OXIDE ABSORPTION	0.15% BY WEIGHT	NO DELETERIOUS EFFECTS

FIGURE 12. EPOXY-SILICONE POLYMERS

**PRESUMED ADVANTAGES**

**BETTER ETHYLENE OXIDE TOLERANCE AND
BETTER DIELECTRIC PROPERTIES THAN
CONVENTIONAL POLYURETHANES**

characteristic of several known polymer systems into a single composite polymer can amplify or nullify traits of the individual systems. Although this approach is largely empirical, it has yielded significantly improved materials. Developing more efficient means to manufacture these materials will permit a more detailed evaluation and provide potting and coating resins with properties much closer to those which are required.

FIGURE 13. URETHANE-SILAZANE POLYMERS



NON-METALLIC MATERIALS

By

James E. Curry

SUMMARY

Cryogenic Insulation. The development of a novel cryogenic multilayer insulation system with micrometeoroid protection capabilities is described. The insulation consists of alternating plastic foam spacer layers and aluminized Mylar reflective layers. Each aluminized Mylar layer is applied under controlled tension by a tape wrapping process and the exterior of the insulation is covered by a resin-impregnated glass fabric which protects the insulation from mechanical damage and serves as the primary micrometeoroid bumper. Large calorimeter test data for several versions of this insulation indicate attractive thermal performance and ease of purging and evacuation. Hypervelocity impact studies have demonstrated that the insulations will provide a measure of protection against micrometeoroid damage to the tank.

Adhesives Research. The total adhesives research effort is summarized with reference to supporting research contracts which supplement parallel inhouse studies now underway on critical aspects of adhesive technology. The goal of this program is to provide new or modified adhesive materials and to identify the optimum conditions for their application, curing and use. As an example of the total effort, a single program on polyurethane adhesives is discussed in detail. Significant data have been obtained on the response of these materials to various aging environments. The aging response of the adhesive applied to aluminum adherends is affected by the presence of primers. The role of various primers is an integral part of this study.

Membrane Diffusion Theory. The permeation of gases and vapors through polymeric seals and films is a subject of wide interest in the space program. This phenomenon frequently occurs under conditions which involve concentration and/or time dependent diffusion coefficients. Some recent theoretical developments are reviewed which indicate that purely concentration-dependent effects can now be treated by an extension of the time lag theory. In ideal cases where time dependent effects are secondary, the nature of the concentration dependence of the diffusion coefficient can be inferred by simple time lag experiments.

CRYOGENIC INSULATION DEVELOPMENT

The micrometeoroid problem will be of increasing concern for space missions of extended duration. The best efforts so far to simulate the micrometeoroid hazard have indicated that many of the micrometeoroid bumper materials are identical or similar to components of several cryogenic insulation systems now in use or under development. In view of this fact, a program is underway in collaboration with Goodyear Aerospace Corporation to combine the insulation and micrometeoroid protective functions into a single composite material.

The initial goals of this effort are summarized in Table I. Certainly, insulations of even higher performance are needed, and these goals are visualized purely as evolutionary steps in that direction. The physical nature of the insulation

TABLE I. INITIAL INSULATION GOALS

1. Maximum vacuum heat leak = 0.789 W/m^2 ($0.25 \text{ Btu/ft}^2\text{-hr}$)
2. Maximum weight = 2.44 kg/m^2 (0.5 lbs/ft^2)
3. Prevent penetration by hypervelocity particles at 9144 m/s ($30\,000 \text{ fps}$) in the 10^{-5} to 10^{-1} g mass range.
4. No internal air or moisture condensation
5. Ability to withstand 506°K (450°F) outer skin ascent conditions
6. Provide insulation under both prelaunch and launch conditions.

was not specified. The first materials evaluated were a variety of low density [32 kg/m^3 (2 lb/ft^3)] polyurethane foams. Although no plastic foams are known which provide the required thermal performance, it was suspected that a foam would be used in some fashion in the final insulation configuration. This preliminary work with foams also served to check the calorimetric devices and techniques that were used later in the program.

The work on foams demonstrated that they are partially transparent in the infrared range. Although this is not surprising, the magnitude of the effect in the low density foams studied in this program was somewhat alarming. A variety of mineral opacifiers were added to various foam pre-mixes to minimize this effect. These additives were not effective at levels that would avoid prohibitive conduction losses.

The best thermal performance obtained from foams was through the use of metallic additives to simulate multilayer characteristics. Conductivity values below $0.00144 \frac{\text{J}}{\text{m} \cdot \text{K} \cdot \text{sec}}$ ($0.01 \frac{\text{Btu-in}}{\text{ft}^2 \cdot \text{F-hr}}$) were obtained with some of these systems in the 32 kg/m^3 (2 lb/ft^3) range. This is near the attainable limit of known foam systems of practical density and strength. The possibility of further improvement hinges upon some spectacular developments in plastic foam technology. At the present time it is not evident what form these developments would take.

The most obvious remaining route to higher performance insulation is the reflective multilayer approach. Two well known systems of this type are shown in Figure 1. The supremacy of this type of

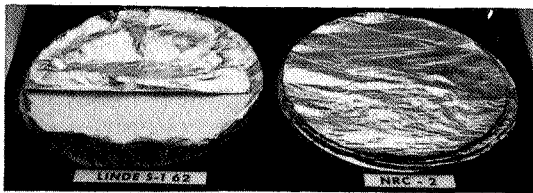


FIGURE 1. REFLECTIVE MULTILAYER INSULATION MATERIALS

insulation under vacuum conditions when compared with other passive systems now available is unquestioned, but purging or evacuation is required to provide reasonable thermal efficiency under pre-launch conditions. The physical form of the insulation makes it difficult to evacuate and the insulation is difficult to attach to the exterior of complex tanks without losing some of its thermal efficiency.

This program has resulted in a method of applying multilayer insulation that promises to minimize these problems. At present, a tape-wrapping process is used to apply aluminized mylar reflective layers over resilient foam spacers. The

6.35μ thick ($1/4$ mil) aluminized Mylar tape is 1.27-cm ($1/2\text{-inch}$) wide and is wrapped over the foam spacers in a polar pattern. A modified filament winding machine keeps the tape under controlled tension (Fig. 2). Foam spacer layers are applied by lightly cinch-wrapping them around the tank (Fig. 3). The pre-cut gore segments of each spacer layer are bonded lightly over the ends with a contact adhesive.

Some typical calorimeter data for tape-wrapped insulations with various foam spacers are shown in Figures 4-6. They are compared to the Linde S-I 62 insulation under variable compressive loading. Apparent conductivities (Fig. 4) are somewhat higher than the Linde insulation. The conductivity-density product (Fig. 5) is lower in most cases for the tape-wrapped insulations. The heat leak-insulation density product (Fig. 6) seems to suggest a significant advantage for the tape-wrapped insulations. On the strength of these data, tape-wrapped insulations were then applied to the large cylindrical tank shown pictorially in Figure 2 and schematically in Figure 7.

The central 0.762-m ($2 \frac{1}{2}\text{-ft}$) diameter by 1.22-m (4-ft) long measuring section was protected by end guards and separate fill and drain connections were provided for all three sections. This tank was designed to fit in a large vacuum system at Goodyear's Wingfoot Lake Test facility.

Two insulation systems have been tested on this tank with liquid hydrogen as the cryogen. These insulations are shown in Figure 8. Both insulations have identical outer sections, consisting of 37 layers each of foam spacer and tape-wrapped reflector beneath a polyurethane impregnated glass fabric. The ground hold section of one insulation consisted of eleven multilayer combinations which were enclosed in a MAAM (Mylar-aluminum-aluminum-Mylar) vacuum bag. The ground hold section of the other insulation was a sealed Mylar honeycomb layer, comparable to the inner section of the dual seal insulation.

Typical performance data for both insulations are shown in Table II. Vacuum performance of the full multilayer version was outstanding, but after five fill and drain cycles under simulated atmospheric conditions the ground hold performance was very poor. Leakage through the vacuum bag into the ground hold section had occurred. This problem has been encountered in other local and contracted insulation projects. The other insulation with a sealed cell ground hold section proved more reliable

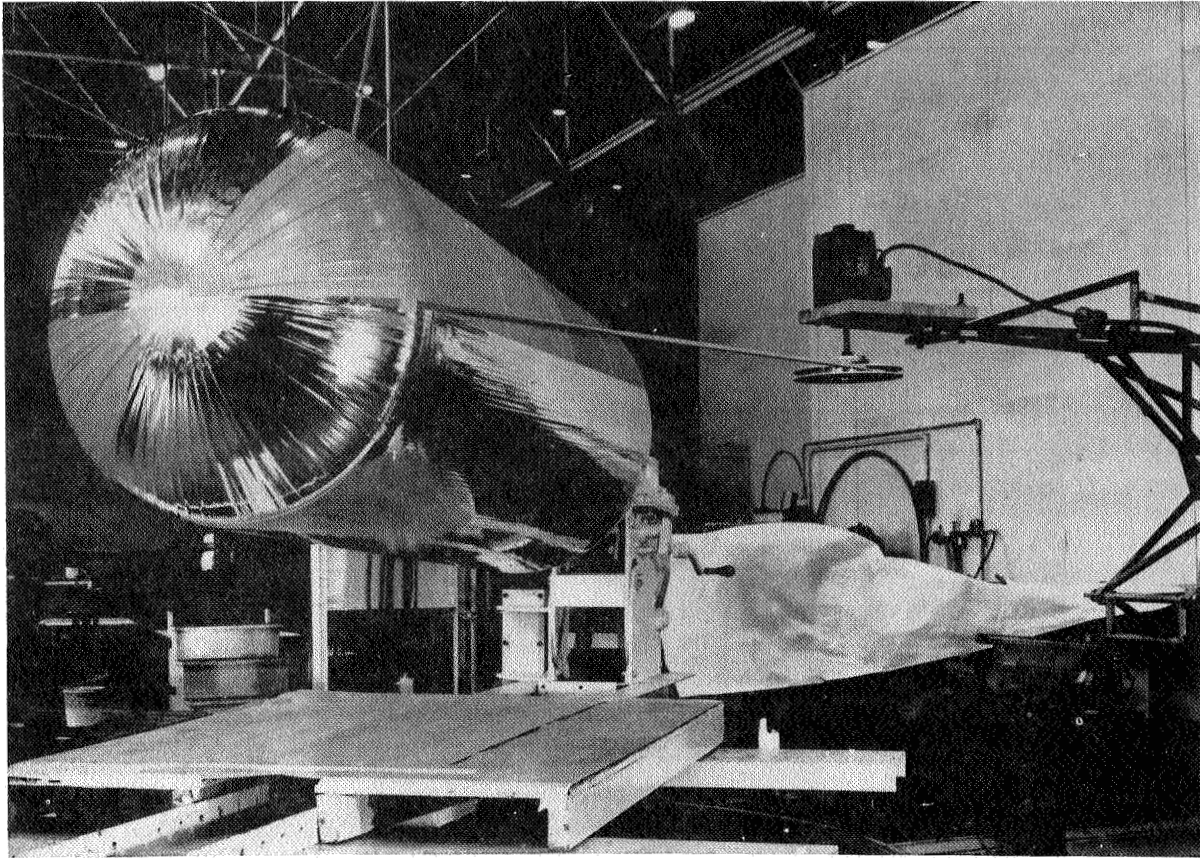


FIGURE 2 INSULATION APPLICATION PROCESS

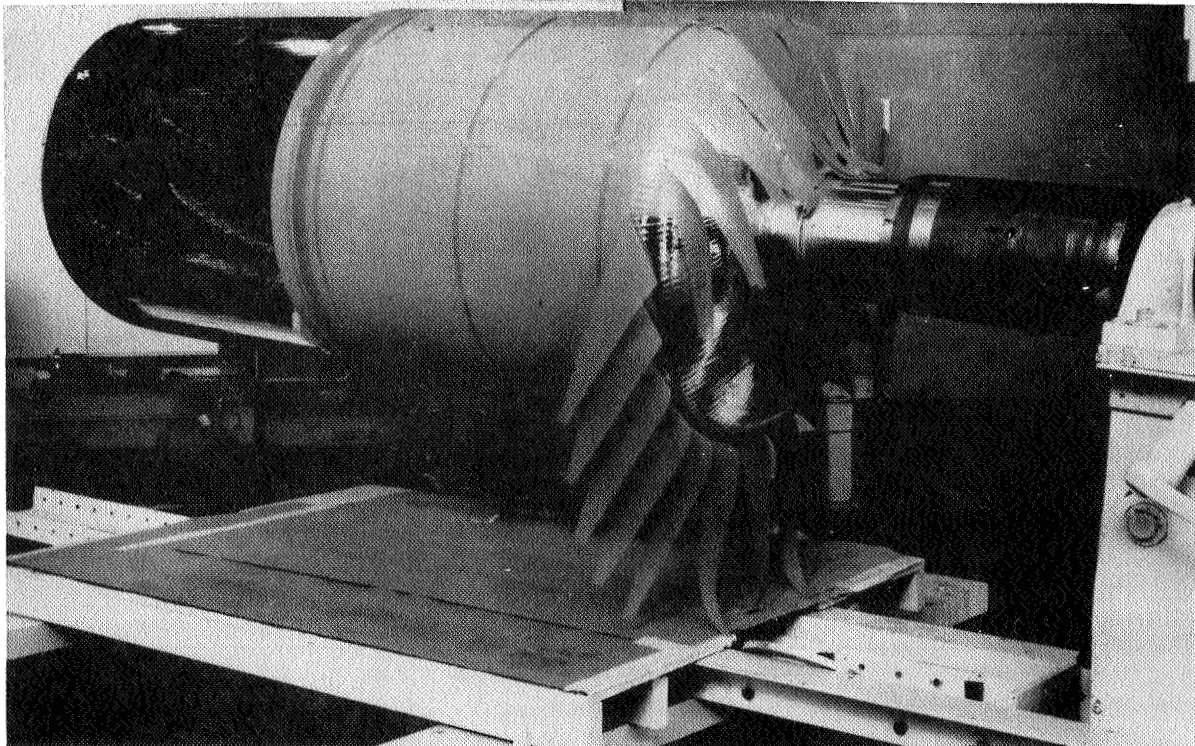


FIGURE 3. FOAM SPACERS SEPARATING INSULATION LAYERS

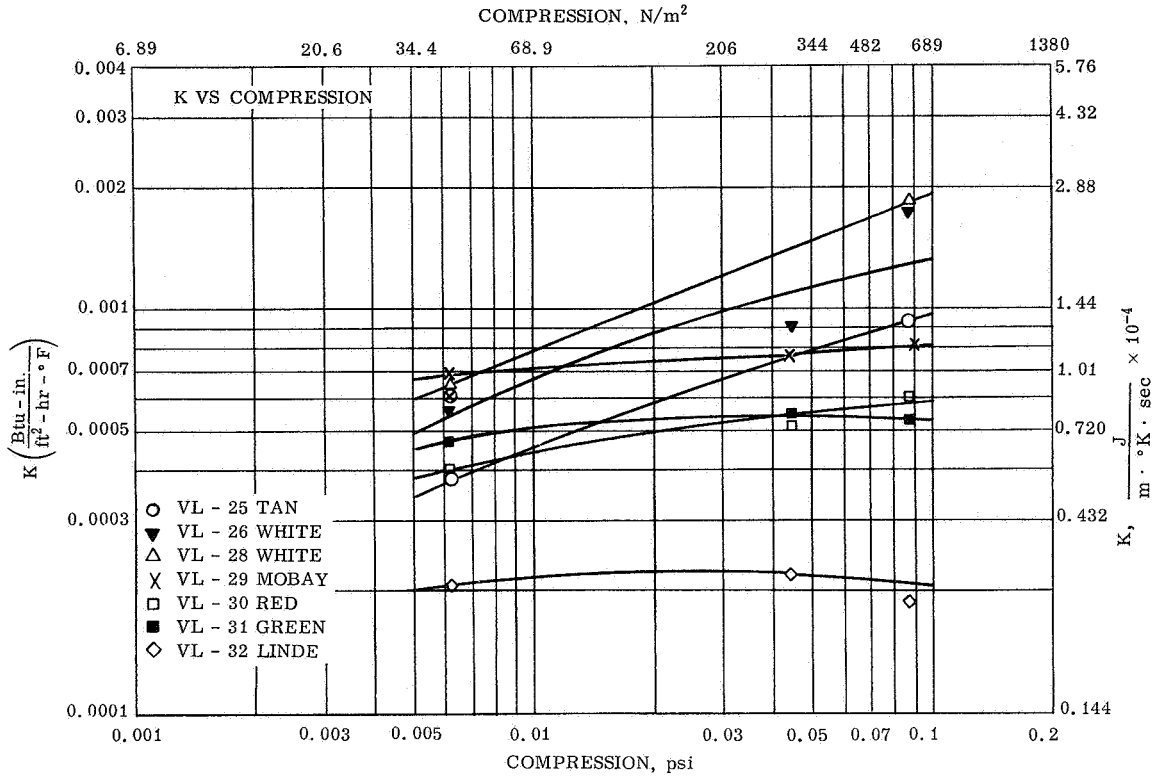


FIGURE 4. EFFECT OF EXTERNAL COMPRESSION ON APPARENT K FOR MULTILAYER INSULATIONS

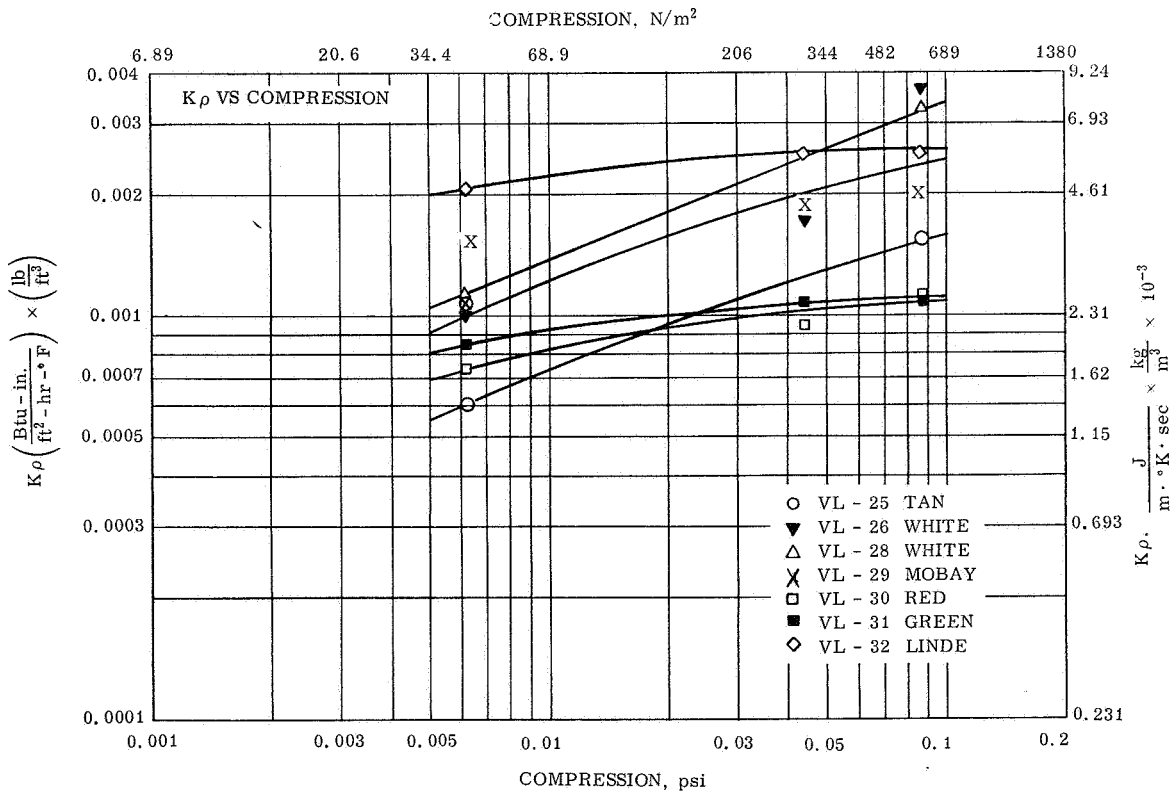


FIGURE 5. EFFECT OF EXTERNAL COMPRESSION ON K_ρ FOR MULTILAYER INSULATIONS

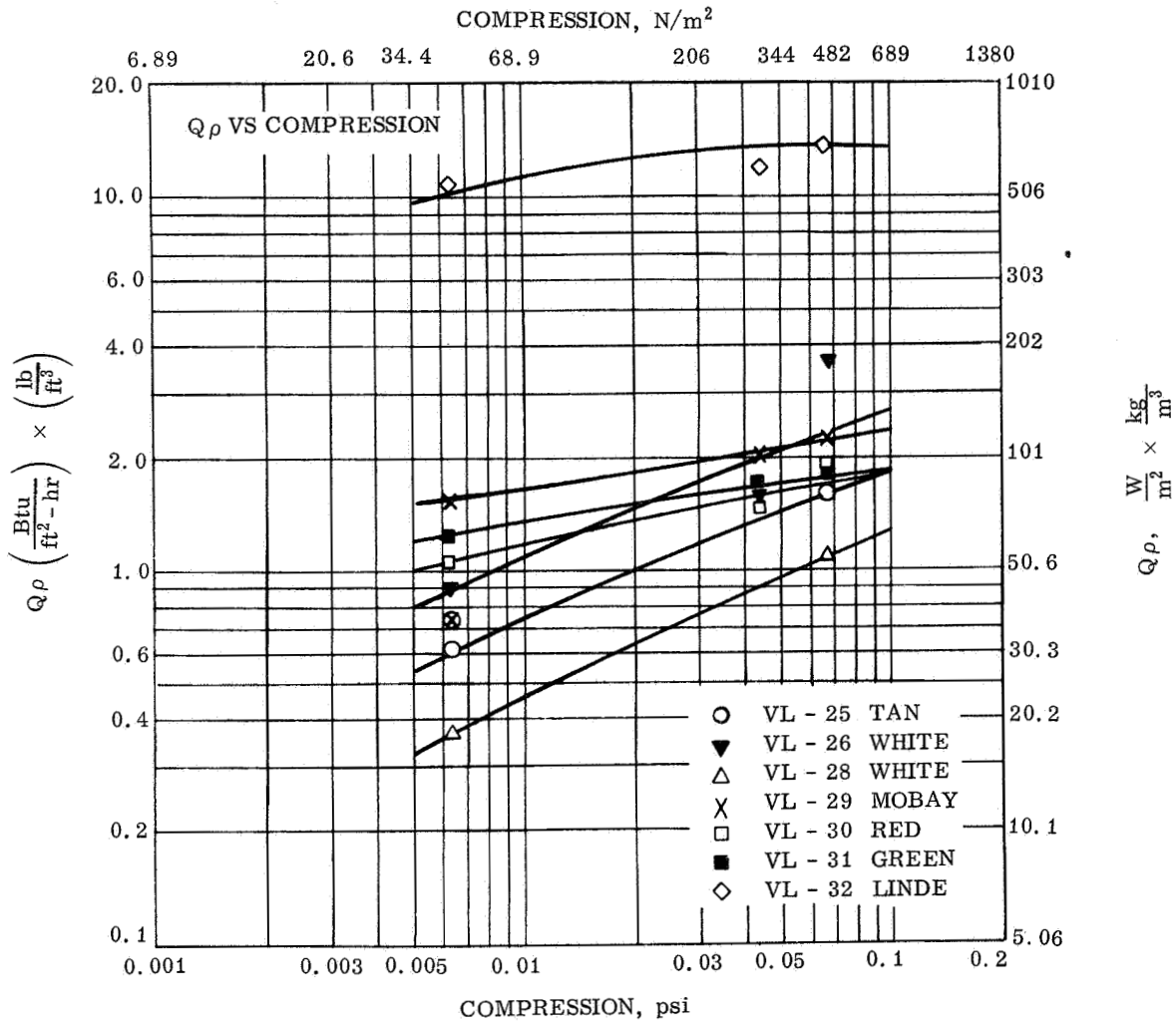


FIGURE 6. EFFECT OF EXTERNAL COMPRESSION ON Q_p FOR MULTILAYER INSULATIONS

in these tests even though its insulation performance is not as good as the ideal performance of the full multilayer version. Until a damage-resistant vacuum bag material is developed, the ideal ground hold performance of the full multilayer insulation cannot be achieved in this fashion.

Since it may be impractical to machine-wrap some tanks, attempts are being made to fabricate this insulation in panels, which will permit its piecewise attachment to the tank by a cinch-wrap contact adhesive combination. Our present contract calls for Goodyear to apply a mutually selected version of this insulation to a large test tank at least 1.78 m (70 in.) in diameter. This tank should be available for testing at this center next May or

June. If the insulation continues to show promise for that size tank, an inflight experiment will be proposed.

Micrometeoroid test work is being done by IIT Research Institute under subcontract to Goodyear. A one week mission for a vehicle 10.7 m (35 ft) in diameter by 30.5 m (100 ft) in length was assumed and calculations based upon generally accepted mass-flux relationships indicated that particles in the 10^{-4} to 10^{-2} gram mass range would be the most probable sources of damage. Every variant of these insulations considered so far has been tested in IIT Research Institute's light gas gun facility with 17 and 70 mg Pyrex projectiles. No damage to the simulated tank structure has been detected when these particles

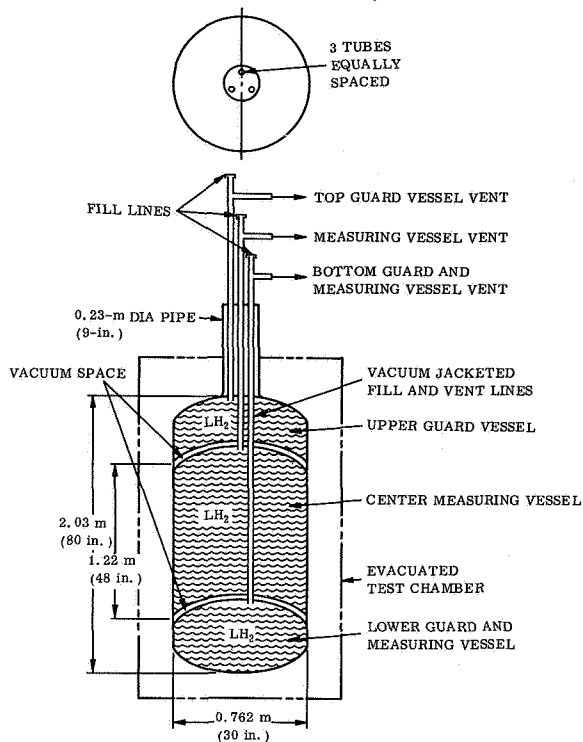


FIGURE 7. CYLINDRICAL CALORIMETER

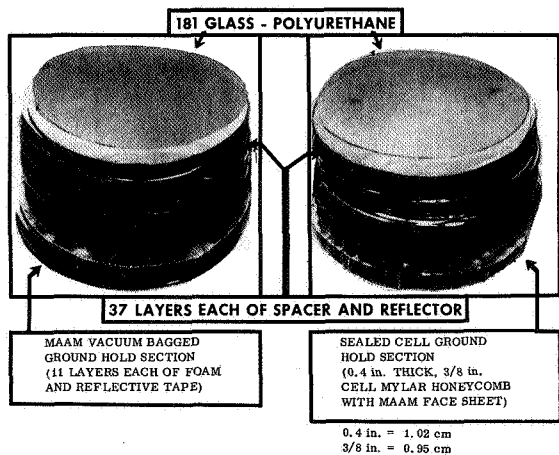


FIGURE 8. TAPE WRAPPED MULTILAYER INSULATIONS

TABLE II. PERFORMANCE OF MULTILAYER INSULATIONS

Test Condition	Vacuum-Bagged Ground Hold Section		Sealed Cell Ground Hold Section	
	K	Q		
	$\frac{J}{m \cdot ^\circ K \cdot sec}$	$\frac{W}{m^2}$	K	Q
	$K \left(\frac{Btu-in.}{ft^2 \cdot ^\circ F \cdot hr} \right)$	$Q \left(\frac{Btu}{hr-ft^2} \right)$		
Vacuum	5.48×10^{-5} (3.8×10^{-4})	0.284 (0.09)	8.65×10^{-5} (6×10^{-4})	0.473 (0.15)
Ground Hold	0.0677-0.0750 (0.47-0.52)	284-316 (90-100)	0.0432-0.0621 (0.30-0.38)	189-236 (60-75)

were impacted on the insulation at velocities ranging from 6710-7930 m/s (22 000-26 000 fps). Despite a limited ability to approximate the true environment, it is believed that these insulations will certainly furnish some protection from micrometeoroids.

Finally, it is recognized that deriving the maximum benefit from superinsulations will require new concepts in tankage support and other hardware to minimize the heat leak from these sources. This problem is being studied in other programs.

In conclusion, this particular system of insulation design and attachment appears to be a realistic means of achieving the desired thermal performance of multilayer insulations while minimizing the practical problems of attachment, installation, purging, and evacuation. This insulation can be purged and evacuated as a single bulk material characterized by a high apparent permeability, and this alone has been a problem with multilayer insulations.

ADHESIVES RESEARCH

Table III is a current listing of major adhesives research and development efforts now being pursued by the Materials Division. A parallel inhouse experimental effort is being conducted on each contract goal. A brief outline follows the approach being followed on each program.

A selective examination of parameters governing performance of polyurethane adhesive systems has been attempted under the first program. These have included variations in the catalyst/resin ratio, variations in cure cycle, effect of humidity level

TABLE III. ADHESIVES RESEARCH

Contract	Title
NAS 8-11958	Optimization of the Performance of a Polyurethane Adhesive System over the Temperature Range of -253° to +93° C (-423° to +200° F)
NAS 8-11068	Development of Structural Adhesives Suitable for Use with Liquid Oxygen
NAS 8-20406	Development of Improved Structural Adhesives for Use over a Wide Temperature Range of -253° to +150° C (-423° to +302° F)
NAS 8-11371	Development of Improved Semi-Organic Structural Adhesives for Elevated Temperature Applications

during the bonding process, effect of bond line thickness, effect of catalyst/resin mix technique, effect of different primers for the adherends, and variations observed between operators. Data were obtained using aluminum lap shear and T-peel specimens.

Liquid oxygen compatible adhesives being sought under the second project require development of fluorocarbon or Teflon-like polymers with adhesive properties. During the past year an internal synthesis program for highly fluorinated polymers was initiated; accomplishments to date have included the synthesis of several fluorinated monomers previously unreported in chemical literature. Polymerization reactions of these monomers are being studied.

A broader spectrum of materials is being studied during the next effort. Improved adhesives without any restrictions on their chemical composition are being developed. These adhesives must be useful at both cryogenic and moderately elevated temperatures. Blends of urethane and epoxy prepolymers with variations in curing systems have comprised the major part of the inhouse effort in this area.

The final program on semi-organic structural adhesives is based upon chelate structures, or organic polymers which contain metal atoms anchored by a particularly stable form of chemical bonding. It was hoped that this same type of bonding

could be activated at the adhesive-metal adherend interface, but this has not yet been confirmed.

This discussion of the overall program covered the major identifiable problem areas in adhesives technology that are under investigation. However, the development of the adhesive is only the beginning. The response of the adhesive system to a variety of environments, both during the bonding process and during the service life of the bonded assembly, must be determined.

Some existing adhesives have undesirable traits and weaknesses that must be examined experimentally. A commercially available polyurethane adhesive in widespread use in our programs is being studied exhaustively in this context because of its inherent temperamentalilty. A major part of this work was concentrated upon the response of this adhesive to aging environments and the evaluation of new primer systems that are now available for this adhesive.

Accelerated aging of polyurethane bonded aluminum lap shear specimens has been accomplished under experimental conditions more severe than normal ambient surroundings. Figure 9 shows data obtained when lap shear specimens bonded with Narmco 7343/7139 adhesive system were stored at 311° K (100° F) at a humidity of 100%. Three series of adherends were used: (a) primed with 3M Company's XC-3901, a silane derivative; (b) primed with Goodyear's G-207 primer; (c) unprimed. These lap shear values were obtained at room temperature. Over a period of 35 days, progressive bond deterioration is evident in all three series. Initial strengths,

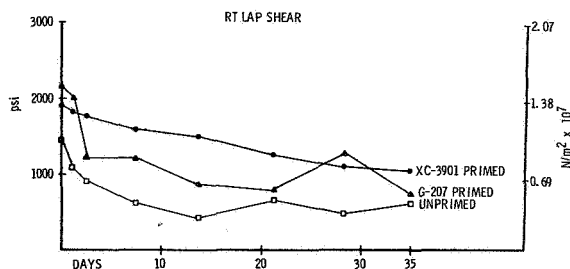


FIGURE 9. LAP SHEAR SPECIMENS (NARMCO 7343/7139) AGED AT 311° K (100° F); 100% HUMIDITY

and, therefore, final strengths for primed specimens were better than for unprimed.

The same relationship holds for specimens tested at 356° K (180° F) (Fig. 10). Bond strengths are again weakened over a 35 day period. The silane derivative, XC-3901, is patently superior to G-207 as a primer at this temperature.

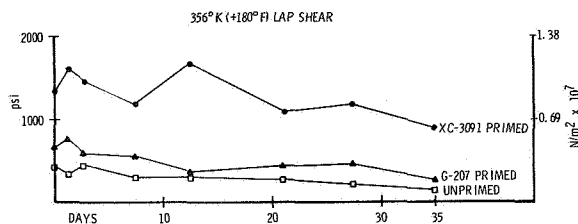


FIGURE 10. LAP SHEAR SPECIMENS (NARMCO 7343/7139) AGED AT 311° K (100° F); 100% HUMIDITY

Specimens tested at 88.6° K (-300° F) (Fig. 11) do not clearly reflect adverse aging effects for primed samples. XC-3901 primed adherends also yield bonds with higher strengths at this temperature than do the G-207 treated adherends.

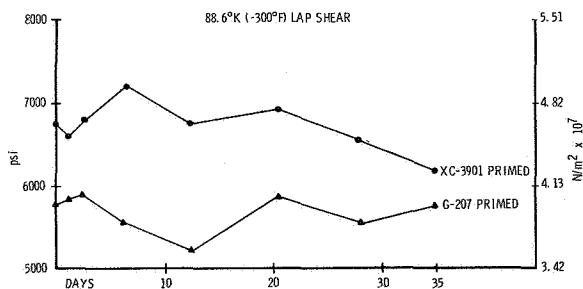


FIGURE 11. LAP SHEAR SPECIMENS (NARMCO 7343/7139) AGED AT 311° K (100° F); 100% HUMIDITY

Since these data were plotted, additional points were obtained in each series at each of three test temperatures. No further bond deterioration was observed after this extended period of aging under this relatively severe experiment.

A similar experiment with milder aging conditions, 294° K (70° F) at 100% humidity, extended over a period of eight weeks with specimens being tested at room temperature and at 77.6° K (-320° F). Results are summarized in Figure 12 for the 77.6° K (-320° F) lap shear tests. The effect of the 294° K (70° F) aging exposure is less severe than the 311° K (100° F) exposure, as would be expected. In these studies another silane primer system, Dow Corning's Z-6020 product, was evaluated and over the full temperature spectrum gave better results than the unprimed specimens or the G-207 primer. Under these conditions, there is no significant deterioration from initial values in the case of the primed samples. This same trend was evident in tests at other temperatures.

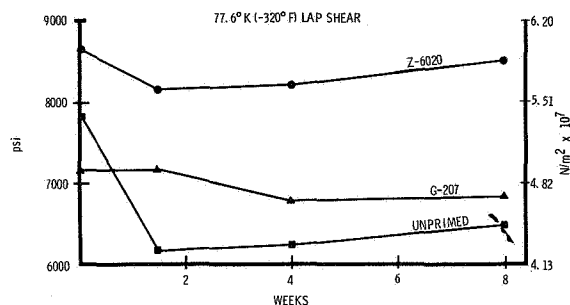


FIGURE 12. LAP SHEAR SPECIMENS (NARMCO 7343/7139) AGED AT 294° K (70° F); 100% HUMIDITY

A long term aging study under ambient, outdoor conditions is also in progress. Aluminum lap shear adherends, bonded with the 7343/7139 adhesive system, are stored outside in a ventilated metal cabinet, protected only from direct precipitation. Figure 13 shows room temperature test results obtained during the first six months on the same three sample types. There is no firmly significant change in the strength values obtained at other test temperatures.

Additional interesting data have demonstrated the beneficial effects of silane-type primers on aluminum lap shear specimens bonded with the 7343/7139 polyurethane adhesive systems. Figure 14 summarizes the results of room temperature tests. Although the values obtained for unprimed specimens were quite good, averaging 1.46×10^7 N/m² (2121 psi), the strength of specimens primed with

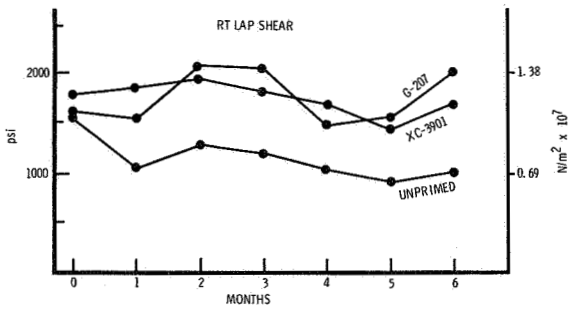


FIGURE 13. LAP SHEAR SPECIMENS (NARMCO 7343/7139) AGED IN AMBIENT OUTDOOR ENVIRONMENT

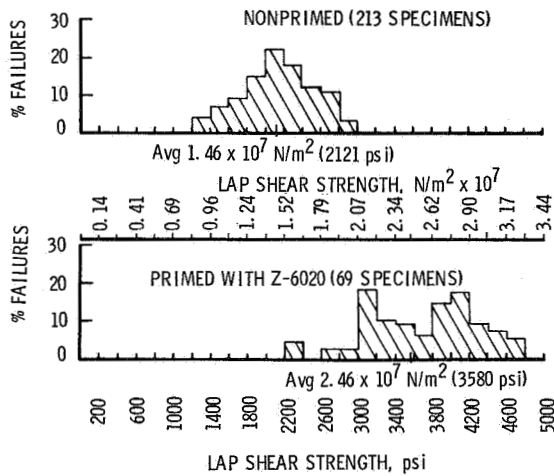


FIGURE 14. DISTRIBUTION OF ROOM TEMPERATURE STRENGTHS (NARMCO 7343/7139)

Dow Corning Z-6020 was considerably improved, yielding an average of $2.46 \times 10^7 N/m^2$ (3580 psi), and more important, a higher minimum value for the series (1.38 vs $0.826 N/m^2 \times 10^7$) (2000 vs 1200 psi). Similar benefits are evident when samples are tested at other temperatures. Figure 15 shows strength distribution obtained at a test temperature of $339^\circ K$ ($+150^\circ F$).

This briefly and partially defines the scope of activities needed to acquire a sound working level of familiarity with one model adhesive system. The most striking observations evident from this work

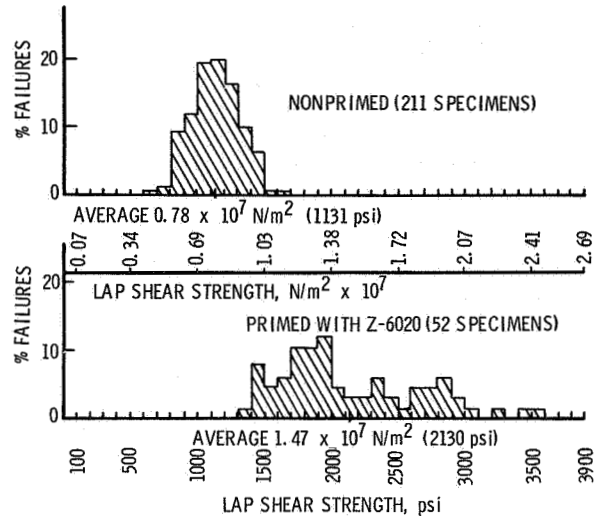


FIGURE 15. DISTRIBUTION OF $339^\circ K$ ($150^\circ F$) LAP SHEAR STRENGTHS (NARMCO 7343/7139)

are the regulatory and beneficial effects of some of the new primers now becoming available. They promote the formation and maintenance of higher bond strengths and apparently can also serve to inhibit strength degradation by the dual effects of temperature and humidity. Finally, it is clear that the effect of an aging environment on an adhesive bond is a function of the service conditions to which the bond will ultimately be exposed.

MEMBRANE DIFFUSION THEORY

Permeation is a recurring environmental problem in using plastic films, bladders and other shapes. Generally polymers or plastics are characterized by permeation rates much higher than metallic components of equivalent geometry. A great amount of work has been and is being done by others in this field. The effort discussed here is an attempt to combine some isolated theoretical developments which promise to greatly simplify the study, analysis and prediction of permeation and diffusion effects.

The overall permeation process through membranes is usually considered to take place in three steps [1]: (1) The penetrant dissolves at the membrane face bordering the zone of highest concentration or pressure, (2) Penetrant molecules then move by activated diffusion through "holes" created in the polymer matrix by the random thermally induced motion of polymer chain segments, (3) At the

downstream or lower concentration face, the penetrant is desorbed.

The diffusion step is usually the rate-controlling phase of the overall process and it is the step most sensitive to variations in polymer and penetrant structure. Thus, it is desirable to study only the diffusional aspect of the overall process.

It is intuitively evident from the preceding argument that steady state permeation measurements do not readily permit separate analysis of solubility and diffusional effects. This can be done easily by transient state permeation measurements if the diffusion coefficient (D) is not a function of penetrant concentration and is not altered by other time dependent processes. This so called time lag approach was developed by Daynes [2] and has been used by numerous other authors [3, 4]. The diffusion coefficient (D) is defined in Fick's Laws of Diffusion (Fig. 16) for unidirectional diffusion in the x direction where J = the mass flux of penetrant per

unit membrane area in the direction of the concentration gradient that is the driving force, C = concentration, and t = time.

To briefly outline the time lag theory, consider a semi-infinite membrane of thickness l which is suddenly exposed on one face to a penetrant concentration C₂ while the downstream face is maintained at zero concentration. There will be a transient period preceding the development of steady state conditions. The boundary and initial conditions are given in Figure 16.

Mathematically the total concentration at any point within the membrane can be considered the sum of two separate concentrations as specified in Figure 17. In effect, C_a is assumed to be position dependent only while C_b incorporates all of the time dependency of this transient state. The boundary and initial conditions for C_b are identical to those for

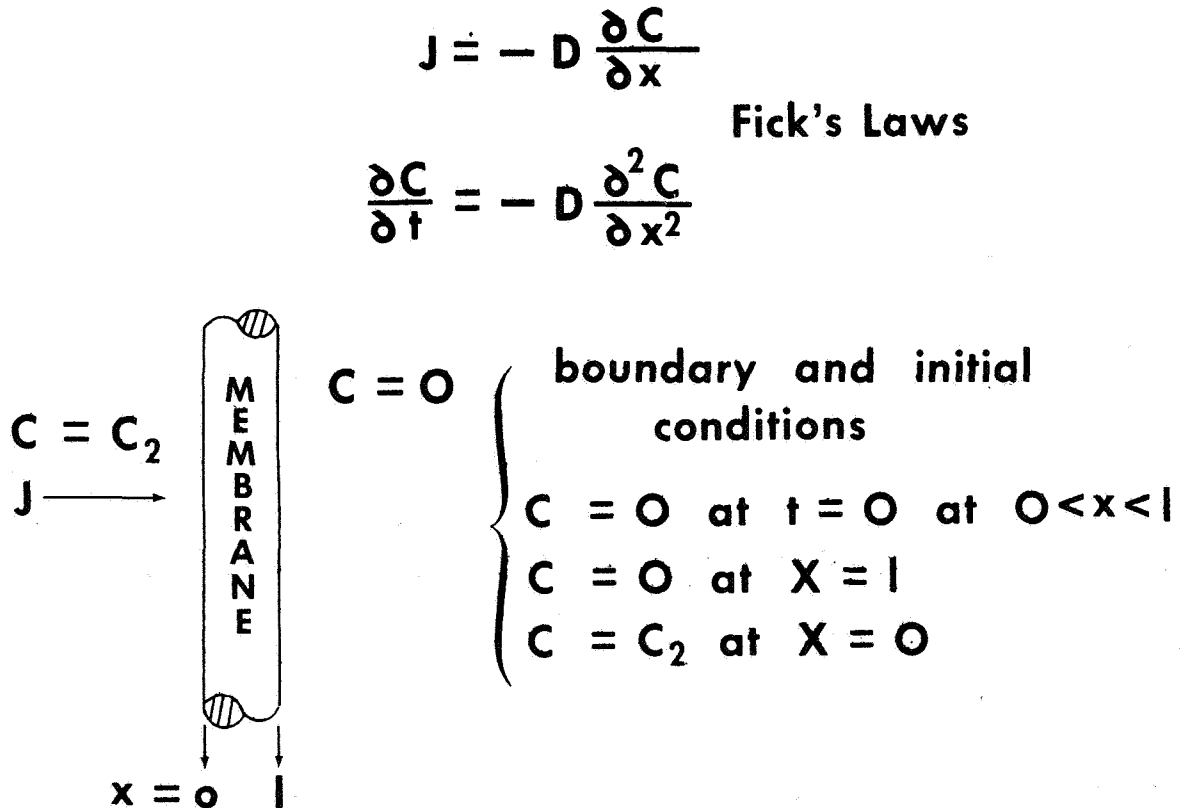


FIGURE 16. DIFFUSION THROUGH MEMBRANES

if $C = C_a + C_b$

$C_a = 0$ at $x = 1$	$C_b = \frac{-C_2(1-x)}{1}$ at $t = 0$
$C_a = C_2$ at $x = 0$	$C_b = 0$ at $t = \infty$
$C_a = \frac{C_2(1-x)}{1}$ for $0 < x < 1$	$C_b = 0$ at $x = 0$
	$C_b = 0$ at $x = 1$

$$C_{x,t} = C_2 \left[\frac{1-x}{1} - \frac{2}{\pi} \sum_{n=1}^{\infty} \frac{1}{n} \sin \frac{n\pi x}{1} \exp \left(\frac{-Dn^2\pi^2 t}{1^2} \right) \right]$$

FOURIER SOLUTION

at large t (steady state):

$$C_{s(x)} = \frac{C_2(1-x)}{1}$$

FIGURE 17. FOURIER MASS TRANSFER SOLUTION

temperature in the analogous heat transfer problem where a semi-infinite slab initially at a uniform temperature is plunged into a "zero" temperature environment [5]. The equation ultimately obtained for the concentration as a function of both time and position is the Fourier Solution (Fig. 17). The contribution of the summation term decreases with time and the steady state concentration distribution ($C_{s(x)}$) is obtained.

Now, assume that the total mass flux issuing from the downstream $x = 1$ membrane area (A) accumulates in a hypothetical volume (V) until penetrant concentration C_g is attained at a time t (Fig. 18).

The rate of penetrant concentration (C_g) increase in a hypothetical downstream volume (V) can be related to Fick's first law as shown in Figure 18. The concentration gradient is obtained by differentiation of the solution for $C_{x,t}$ in Figure 17 and

evaluating dC/dx at $x = 1$. This permits the estimation of C_g at large values of time (t), which would be well within the steady state permeation realm.

Note that it is possible to solve this equation for t . If steady state conditions had existed from the beginning of the experiment ($t = 0$), some shorter time designated t^* would have been required to develop the same concentration C_g that was developed in the longer experiment spanning the transient state. Equating these expressions for C_g permits the calculation of the time lag L that is defined as $t - t^*$.

In principle, the time lag approach permits calculation of a constant diffusion coefficient from the membrane thickness and observed time lag in spite of the simultaneously-occurring solubility effects. The graphical interpretation of the time lag is shown in Figure 19. Deviations from this relationship have been observed in many cases of practical interest. These instances have been rather indiscriminately labeled "non-Fickian diffusion" by some investigators.

If time dependent relaxation effects in the membrane material are relegated to a minor role, one

$$V \int_0^t \frac{dC_g}{dt} = [J_t]_{x=l} A = -AD \left(\frac{dC}{dx} \right)_{x=l}$$

$$C_g = \frac{DC_2 A}{Vl} \left[t + 2 \frac{l^2}{D\pi^2} \sum_{n=1}^{\infty} \frac{(-1)^n}{n^2} \exp \left(\frac{-Dn^2 \pi^2 t}{l^2} \right) \right]$$

$$\text{or } C_g = \frac{DC_2 A}{Vl} \left[t - \frac{l^2}{6D} \right] \text{ at large } t$$

$$\frac{C_g V}{t^*} = \frac{DC_2 A}{l} \quad ; \quad C_g = \frac{DC_2 t^* A}{Vl}$$

Equating Values For C_g :

$$t - t^* = L = \frac{l^2}{6D} \quad ; \quad D = \frac{l^2}{6L}$$

FIGURE 18. TIME LAG APPROACH

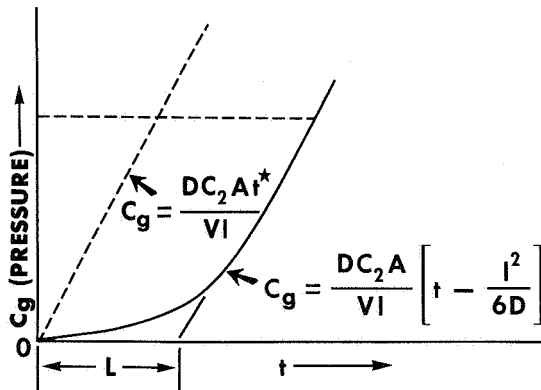


FIGURE 19. GRAPHICAL SIGNIFICANCE OF TIME LAG

possible explanation for these deviations would be that there exists a variation of the diffusion coefficient with penetrant concentration (Fig. 20). D_c

$$\frac{\partial C}{\partial t} = \frac{\partial}{\partial x} \left(D_c \frac{\partial C}{\partial x} \right)$$

where $D_c = f(D_0, C)$
 $D_c = D_0 (1 + aC)$
 or $D_c = D_0 \exp(bc)$, etc.

FIGURE 20. FICK'S SECOND LAW FOR CONCENTRATION-DEPENDENT DIFFUSION COEFFICIENT (D)

is a variable diffusion coefficient, and D_0 is a hypothetical "zero concentration" diffusion coefficient (Fig. 20). Although a steady state permeation rate is attained in concentration dependent systems, the experimentally observed time lag is not as straightforwardly related to the diffusion coefficient as it was in the earlier case.

One notable contribution in dealing with concentration dependent situations has been made by Holstein [6] who pointed out that the Fourier solution to Fick's first law equation can be subjected to the series transformation in Figure 21 [7]. Substituting

in J_t for y and Z , another version of the flux equation is obtained in which the time parameter (t) is in the denominator of the negative exponent. Rearranging and taking the logarithm of both sides permits the conclusion stated in Figure 21.

$$\begin{aligned}
 [J_t]_{x=l} &= \frac{DC_2}{l} \left[1 + 2 \sum_1^{\infty} \cos n\pi \exp \left(- \frac{Dn^2 \pi^2 t}{l^2} \right) \right] \\
 &\downarrow \\
 \text{apply } \sum_{-\infty}^{\infty} \exp \left(- \frac{\pi n^2}{Z} \right) \exp 2\pi iny &= \sqrt{Z} \sum_{-\infty}^{\infty} \exp \left[- \pi(n+y)^2 Z \right] \\
 \text{by setting } y = 1/2 \text{ and } Z &= \frac{l^2}{\pi D t} \\
 &\downarrow \\
 [J_t]_{x=l} &= 2C_2 \sqrt{\frac{D}{\pi t}} \exp \left(- \frac{l^2}{4Dt} \right) = \frac{V}{A} \frac{dC_g}{dt} \\
 \text{conclusion: } \frac{1}{t} \text{ versus } \ln \left(\frac{dC_g}{dt} \sqrt{t} \right) &\text{ plot has slope } \left(\frac{-l^2}{4D} \right)
 \end{aligned}$$

FIGURE 21. HOLSTEIN TRANSFORMATION VALID FOR SHORT TIME MEASUREMENTS

Thus, if the diffusion coefficient is constant, a plot of $\ln \frac{dC}{dt} \sqrt{t}$ versus $1/t$ should be a straight line of slope $\left(\frac{-l^2}{4D} \right)$. More importantly, if the diffusion coefficient is concentration dependent, the plot can be extrapolated to $t = 0$ and the slope at that point may be used to calculate D_0 , the zero concentration diffusion coefficient. This is one of the parameters needed to define the variability of the true diffusion coefficient with concentration.

A second contribution has been made by Frisch [8] who has defined the significance of the time lag in concentration dependent systems. The two key equations that result from his treatment are shown in Figure 22. D_c is some inferred or assumed function of D_0 and C , while $C_s(x)$ is the position-dependent steady state concentration. In principle, the first equation is used to obtain C_s as a function

$$\begin{aligned}
 \int_{C_s(x)}^{C_2} D_c dC &= \frac{x}{l} \int_0^{C_2} D_c dC \\
 L &= \frac{\int_0^l x C_s(x) dx}{\int_0^{C_2} D_c dC} \\
 \text{where } D_c &= D_0 (1 + ac) \\
 &\text{or } D_0 \exp (bc) \text{ etc.}
 \end{aligned}$$

FIGURE 22. FRISCH TIME LAG EQUATIONS FOR D VARYING WITH C

of x and that result is used to calculate a time lag which is then compared with experimental observations. The functional form of D_c is known for some membrane-penetrant systems; in many cases the data are represented by equations like those in Figure 22.

Theoretically, the picture is now complete. From a single transient state permeation experiment, the value of D_0 can be calculated using the short-time transform of the Fourier flux equation. Using the time lag measured later in the same experiment, a constant in one of these equations can be adjusted to obtain all of the information necessary

to describe the diffusional process in terms of the concentration dependent differential diffusion coefficient. In spite of the potentially great saving in time and experimental effort offered by this approach, it has been only partially tested in some work reported recently by Meares [9]. Experimental work is being planned to establish if this approach will clarify practical permeation problems. If this line of reasoning can be extended to systems that are complicated by time dependent relaxation effects in the membrane material, an interesting experimental probe would then be available for studying segmental motion in the polymer solid state. Some of the problems discussed previously arise directly from our lack of understanding of the nature, frequency and extent of this segmental motion.

REFERENCES

1. Lebovits, A.: Modern Plastics. Vol. 43, No. 7, 1966, p. 139.
2. Daynes, H. A.: Proceedings of the Royal Society of London (Series A). Vol. 97, 1920, p. 286.
3. Barrer, R. M.: Diffusion In and Through Solids. Cambridge University Press, New York, 1941, p. 18 ff.
4. Jost, W.: Diffusion in Solids, Liquids and Gases. Academic Press, Inc., New York, 1966.
5. Carslaw, H. S.; and Jaeger, J. C.: Conduction of Heat in Solids. Oxford University Press, New York, 1959, p. 92 ff.
6. Holstein, T.: Research Report 60-94411-9-D. Westinghouse Electric Company, December 20, 1951.
7. Courant, R.; and Hilbert, D.: Methods of Mathematical Physics. Second Edition.
8. Frisch, H. L.: Journal of Physical Chemistry. Vol. 61, 1957, p. 93, and Vol. 62, 1958, p. 401.
9. Meares, P.: Journal of Applied Polymer Science. Vol. 9, 1965, p. 917.